MACHINE-LEARNING REVEALS AFTERSHOCK LOCATIONS FOR THREE

IDAHO EARTHQUAKE SEQUENCE

by

Spencer F. Wilbur

A thesis

submitted in partial fulfillment

of the requirements for the degree of

Master of Science in Geophysics

Boise State University

August 2022

BOISE STATE UNIVERSITY GRADUATE COLLEGE

DEFENSE COMMITTEE AND FINAL READING APPROVALS

of the thesis submitted by

Spencer F. Wilbur

Thesis Title: Machine-Learning Reveals Aftershock Locations for Three Idaho
Earthquake Sequences

Date of Final Oral Examination: 18 May 2022

The following individuals read and discussed the thesis submitted by student Spencer F. Wilbur, and they evaluated the student's presentation and response to questions during the final oral examination. They found that the student passed the final oral examination.

Lee Liberty, M.Sc.   Chair, Supervisory Committee

T. Dylan Mikesell, Ph.D.   Member, Supervisory Committee

Blaine Bockholt, Ph.D.   Member, Supervisory Committee

The final reading approval of the thesis was granted by Lee Liberty, Chair of the Supervisory Committee. The thesis was approved by the Graduate College.

DEDICATION

The process of tackling this research project would have been significantly more difficult, and rather impossible, without the help of my patient and resourceful advisors. Dylan Mikesell and Lee Liberty provided me with the necessary knowledge, direction, motivation, and well-timed jokes to get me through to the end. Dylan, thanks for always finding time to answer my relentless questions and fixing my broken scripts. Lee, thank you for being a fountain of geologic information and always leaving you door open. I appreciate you both.

ACKNOWLEDGMENTS

I would like to acknowledge all my committee members for the valuable insight and support throughout my masters. I would like to acknowledge Blaine Bockholt, Dylan Mikesell, and Kristinia Rossavik for spending countless hours picking phase arrivals that assisted this research. I would like to acknowledge Claudio Berti and Larry "TomO" Otheim for getting seismometers deployed in the field. I also need to acknowledge the amazing faculty in the geoscience department for being supportive, available, and providing a genuine sense of community as well as a lot of free coffee. Lastly, I would also like to acknowledge my friends and family, here in Boise and elsewhere. Thanks for keeping me sane.

ABSTRACT

I explore spatial and temporal aftershock patterns related to three instrumentally recorded earthquakes in Idaho -- the Sulphur Peak, the Challis, and the Stanley earthquakes. These three M>5 earthquakes border the eastern Snake River Plain and lie within the Intermountain Seismic Belt and Centennial Tectonic Belt. Using machine learning for event detection and phase picking from local and regional seismic networks, I generate new aftershock catalogs. I locate more aftershocks than in the USGS catalog due to lower signal-to-noise detections. Using my phase picks, I locate aftershocks using a range of velocity models and select a catalog that represents the smallest residuals in hypocenter locations. I compare my results with handpicked phases and previously published velocity models. My 2014-2017 Challis catalog is consistent with the work of Pang et al. (2018), with more high-quality events with similar average vertical error. My one-month aftershock catalog for the 2017 Sulphur Peak earthquake is spatially consistent with the results of Koper et al. (2018); however, I show that my machine-learning approach produced relatively few aftershocks because afterslip events were not matched using a coseismic training dataset. Finally, I locate a factor of five more aftershocks from the 2020 Stanley earthquake when compared to the USGS catalog. I relocate the mainshock using biases computed by differencing my aftershock epicenters with the same aftershocks in the USGS catalog. The revised mainshock location now lies within a large and pronounced aftershock zone. My catalog suggests no motion along the active Sawtooth Fault, but instead I map a new N10W trending fault that accommodated

the mainshock and much of the aftershock slip. I conclude that aftershock catalogs derived from a machine-learning approach can enhance seismic detection and aid in determining the driving mechanisms responsible for a coseismically driven earthquakes.

TABLE OF CONTENTS

LIST OF TABLES

LIST OF FIGURES

LIST OF ABBREVIATIONS

BSU   Boise State University

BRP   Basin and Range Province

CTB   Centennial Tectonic Belt

GC   Graduate College

DMC   Data Management Center

EBLF   East Bear Lake Fault

ERH   Horizontal Residual Error

ERZ   Vertical Residual Error

EQT   Earthquake Transformer

IDOR   Idaho Oregon

INL   Idaho National Lab

ISB   Intermountain Seismic Belt

JPA   Japan Meteorological Agency

SRP   Snake River Plain

STEAD   Stanford Earthquake Dataset

TCFS   Trans-Challis Fault System

TDC   Thesis and Dissertation Coordinator

USGS   United Stated Geological Survey

CHAPTER ONE: INTRODUCTION

Idaho has hosted several large instrumentally recorded earthquakes over the past 50 years. The seismicity has been characterized as both coseismic and aseismic, with both strike-slip and dip-slip inferred fault motions. Three recent M>5 earthquake sequences are the focus of my research. The March 2020 M_w 6.5 Stanley earthquake, the April 2014-May 2017 M_L 5.0 and M_L 4.9 Challis earthquakes, and the September 2017 M_w 5.3 Sulphur Peak earthquake were each recorded with a regional seismic network. Within days of each mainshock, a rapid temporary seismic station deployment provided additional phase arrival information to complement permanent regional network data. Each temporary station was located within about 50 km from the corresponding mainshock, but deployment strategies differed for each sequence. Most temporary stations did not provide real-time data for earthquake catalogs, but were only available for subsequent analyses. Here, with the use of a machine-learning approach, I create new aftershock catalogs and examine aftershock patterns for all three earthquakes using the combined temporary and permanent station networks. From these catalogs, I compare my automated detection approach to hand-picked catalogs for each sequence, which provides a chance to explore station density. I then discuss the aftershock characteristics for the Stanley sequence to provide an improved understanding of active tectonics in Idaho.

Aftershock alignments and moment tensor solutions from each of these three modern earthquake sequences have called into question the nature of large earthquakes in

Idaho (i.e., Koper et al., 2018; Pang et al., 2018; Liberty et al., 2021). The enigmatic nature of presumed fault motions with intersecting faults suggests complex fault zones. Thus, additional aftershock characterization is warranted and required to better understand the regional tectonic setting. Through machine-learning, I increase the number of identified aftershocks to reduce the completion magnitude of each aftershock catalog. From these new catalogs, I aim to improve the understanding of each fault system.

The 2020 Stanley earthquake occurred beneath central Idaho near two previously recorded M≥6 earthquakes that occurred in 1944 and 1945. These events were termed the Seafoam earthquakes (Dewey, 1987). The Stanley mainshock epicenter located northwest of the mapped Sawtooth Fault (Thackray et al., 2013; Figure 1), did not rupture the ground surface, and was felt widely across Idaho. Preliminary assessments suggested left-lateral oblique strike slip motion along an unmapped fault (Liberty et al., 2021; Pollitz et al., 2021). Two years after the mainshock, M>3 aftershocks continue (U.S. Geological Survey, 2022b). I explore nine months of data recorded across a 16-station temporary local network and a permanent regional network. The local network was deployed within days of the mainshock (Liberty et al., 2021) and largely removed by November 2020. I use a combination of the local and regional stations to relocate aftershocks and explore fault motions and interactions. I then compare the machine-learning aftershock locations to the hand-picked catalog obtained using the same regional and local stations for quality assurance. In addition, I use the changing temporary seismic network to assess the value of the different deployment strategies.

The 2017 Sulphur Peak earthquake occurred near Sulphur Springs, Idaho, and was felt in Idaho, Utah, and Wyoming (Koper et al., 2018). The mainshock occurred near the East-Bear Lake normal fault (EBLF) (Evans et al., 2003). The aftershock sequence lasted from September through October 2017 and was highly energetic. In other words, a significant number of aftershocks with unexpectedly high magnitudes were recorded following the main shock. With the use of both temporary local and permanent regional networks, Koper et al. (2018) related many of these aftershocks to fluid-induced afterslip. I explore the one-month 8-station local network that was deployed within two weeks of the Sulphur Peak mainshock (Koper et al., 2018) to compare hand-picked and machine-learning aftershock catalogs in the presence of both coseismic and aseismic moment releases.

In April 2014, a M_L 4.8 earthquake occurred near the town of Challis, Idaho (Pang et al., 2018). The earthquake epicenter was located about 25 km northwest of the surface rupturing 1983 M_s 6.9 Borah Peak earthquake, near the northern termination of the Lost River fault (Crone & Haller, 1991). The sequence lasted for a few months and was regionally felt. Beginning in January 2015, another series of aftershocks initiated with a M_L 5.0 earthquake, centered approximately 20 km to the southeast of the April 2014 earthquake. Unlike the Borah Peak normal faulting sequence, the Challis earthquakes did not have normal fault motions. I explore the use of an eight-station temporary local network deployed after the first mainshock in 2014. The network remained active until the end of 2014, when all but one temporary station was removed (Pang et al., 2018). Like the Sulphur Peak aftershock sequence, I compare hand-picked and machine-learning aftershock catalogs.

I am motivated by three hypotheses. First, machine-learning, specifically the Earthquake Transformer (EQT) algorithm (Mousavi et al., 2020), provides a robust method for low signal-to-noise earthquake detection and phase picking in Idaho and surrounding regions. Second, by increasing the number of local stations that are deployed immediately after a large earthquake, an improved aftershock catalog can be obtained via machine-learning on "big local data". Third, through machine-learning, the addition of quality events detected beyond the hand-picked catalogs will improve fault interpretations for each aftershock sequence and reduce the completion magnitude. For all aftershock sequences, I test the accuracy of EQT by comparing to hand-picked earthquake catalogs. I also compare my interpretations to those of previously published aftershock studies.

In Chapter 2, I outline the geologic and tectonic background surrounding the Stanley, Sulphur, and Challis regions. In Chapter 3, I introduce the traditional methods used for aftershock detection and catalog construction. I then introduce the EQT machine-learning approach and compare the two processing strategies. In Chapter 4, I introduce two local velocity models used to locate aftershocks. I use these velocity models to locate events detected by EQT using Hypoinverse (Klein, 2014) and generate new earthquake hypocenter datasets for each aftershock sequence. I then quality control these hypocenter datasets to create high-quality, low-error catalogs and compare the hypocenter results to USGS catalog residuals. In Chapter 5, I use these new EQT-based catalogs for interpretation, and I compare my results to previous catalogs constructed using the traditional methods (e.g., U.S Geological Survey, 2022a). I highlight the similarities and differences compared to previous interpretations. In Chapter 6, I provide

a detailed interpretation of the Stanley aftershock sequence and summarize the machine-learning results for the Sulphur and Challis sequence. Finally, in Chapter 7, I present concluding statements from my thesis.

CHAPTER TWO: GEOLOGIC AND TECTONIC BACKGROUND

The Stanley, Sulphur, and Challis regions lie within the Basin and Range Province (BRP) of the western United States (Figure 2.1). The BRP is a 750 km wide extensional tectonic province with Miocene to recent fault activity (Eaton, 1982). This province extends from Montana to Arizona and encompasses much of Idaho, Nevada, and Utah. Within the northern and eastern regions of the BRP, two subregions have been characterized. The Intermountain Seismic Belt (ISB) defines the eastern zone of BRP seismicity (Smith & Sbar, 1974). In Idaho, this zone coincides with the eastern border of Wyoming and Utah. The Sulphur Peak earthquake lies within the ISB. The northeast-trending Centennial Tectonic Belt (CTB) represents a band of seismicity along the northern BRP margin in Idaho and Montana (Stickney et al., 1987). This zone has hosted some of the largest BRP earthquakes, including the 1959 M7.3 Hebgen Lake earthquake and the 1983 M6.9 Borah Peak earthquake. The Stanley and Challis regions lie within the CTB.
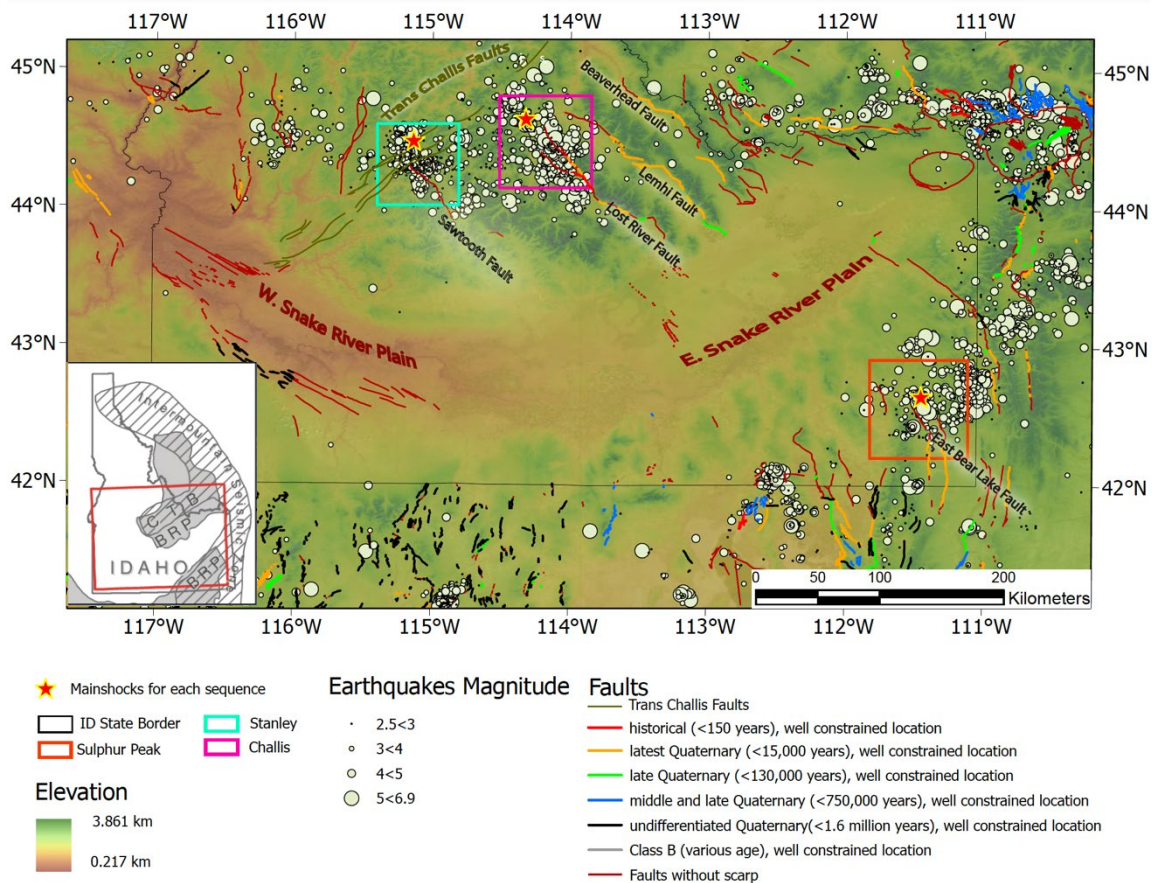
Figure 2.1   Topographic map showing M>2.5 earthquakes since 1981. Faults are from the Quaternary Fold and Fault Database (U.S Geological Survey, 2022c) and the Trans-Challis Faults System (TCFS) is from Lewis et al. (2012). Inset map shows BRP (gray shading), CTB, and ISB (diagonal lines) extent (modified from Liberty et al., 2021). Aftershocks and historical seismicity are from the U.S. Geological Survey comprehensive earthquake catalog (U.S. Geological Survey, 2022b).

There is a parabolic-shaped pattern of seismicity that centers on the axis of the eastern Snake River Plain (SRP) and the Yellowstone Plateau (Anders et al., 1989) (Figure 2.1). This seismicity surrounds a region of aseismicity that includes the eastern SRP. The SRP represents a modern-day topographic low overprinted on the BRP. The SRP formation is related to the passage of the Yellowstone hotspot that emplaced mafic materials within the crust, then subsequent deflation (Armstrong et al., 1975). While geodetic data suggest variable motions within the SRP and BRP, it is unclear how strain

partitioning through time has impacted seismicity within each of the provinces and seismic zones (e.g., Payne et al., 2013).

Within the CTB of Idaho, four subparallel northwest-striking normal faults contain Precambrian and Paleozoic igneous, sedimentary, and metamorphic rocks within their respective ranges (Stickney & Bartholomew, 1987). These faults are identified as the named faults in the northern center of Figure 2.1. Tertiary and younger sediments occupy the basins, and the relief between the mountain tops and the basin floor defines the long-term slip rate for these faults (Crone & Haller, 1991). Paleoseismic and geomorphic indicators show Quaternary activity and there are large tectonic scarps related to these faults (Scott et al., 1985; Thackray et al., 2013).

The Stanley earthquake and aftershock sequence lies mostly to the north of the Sawtooth fault (Figure 2.1), and west of the Sawtooth Fault lies the Cretaceous Idaho Batholith that defines the western limits of the BRP and CTB. The east-dipping Sawtooth normal fault extends at least 60 km, but the total length and displacement is debated due to the lack of fault outcrop observations to the northwest and limited subsurface characterization. Thackray et al. (2013) documented four- to nine-meter high scarps that displace 11-14 ka glacial deposits. They also identified two- to three-meter high scarps that displace Holocene alluvial deposits. They noted that two or three postglacial surface rupturing events have occurred, suggesting that there are discrete fault segments. They estimated a Holocene slip rate of 0.5-0.9 mm/year, higher than the long-term Quaternary slip rate estimate of <0.2mm/year (Personius et al., 2009). Length-magnitude scaling relationships and a two- to three-meter high surface rupture suggest that the Sawtooth fault is capable of supporting a M7 earthquake. The relationship between the oblique

strike-slip 2020 Stanley earthquake sequence and the Sawtooth fault is poorly understood (Liberty et al., 2021). The Stanley epicentral region lies near its intersection with the northeast-trending faults of the Trans-Challis fault system (TCFS) and these faults may influence regional seismicity patterns.

The Sulphur Peak earthquake and aftershocks were centered to the south of the Aspen Range and northeast of the EBLF (Figure 2.1). Evans et al. (2003) mapped the EBLF as a steep west dipping normal fault, possibly becoming listric at depth. The EBLF exhibits Quaternary-age fault scarps along three of its segments; as well as paleoseismic evidence for five to seven surface rupturing earthquakes (M6.8-M7.2) in the last 40,000 years (Payne et al., 2013). The seismicity following the 2017 Sulphur Peak mainshock occurred within a short window of time, approximately one week, and the energy released in this window of time exceeded what was expected based on the magnitude of the mainshock (Båth, 1965). Within 10 days of the Sulphur Peak mainshock, 16 of 17 earthquakes that occurred had exceeded the predicted maximum aftershock magnitude. This observation along with the rapid spatial expansion of aftershocks over ~10km to the SE, suggests there are additional driving mechanisms apart from the cosiesmic mainshock (Koper et al., 2018). The exact driving mechanism of seismicity in Sulphur Peak is enigmatic and does not reflect seismic trends occurring in the CTB or BRP (Payne et al., 2013). Previous interpretations have suggested that southeastern Idaho might be a region with slow slip or creep events, but the cause of aseismic creep is not entirely understood (Peng & Gomberg, 2010).

The Challis earthquake and aftershock sequence was centered to the north of Challis, Idaho, near the west-dipping Lost River fault (Figure 2.1). The Lost River fault,

like the EBLF and Sawtooth fault, is a northwest trending normal fault that has accommodated significant vertical displacement along six segments (Crone & Haller, 1991). The Lost River Fault and intersecting TCFS to the northwest controls a syn-volcanic basin that accommodated Eocene extension and subsidence in the region (Kiilsgaard et al., 1986). While there is no direct evidence for active motion on faults that lie within the graben, prior paleoseismic indicators suggest Holocene activity in the central region of the Lost River Fault, including the M_s 7.3 Borah Peak earthquake in 1983 (Bello et al., 2021; DuRoss et al., 2022; Scott et al., 1985). This earthquake epicenter was located near the southeastern end of the observed surface rupture. The hypocenter was reported at 16 km depth, near the edge of the brittle-ductile transition zone (Smith et al., 1985). Following the Borah Peak earthquake, aftershocks migrated to the northwest, but not along any known Quaternary faults (Pang et al., 2018). The 2014 Challis sequence has been proposed as a continuation of the 1983 Borah Peak earthquake aftershock sequence (Pang et al., 2018).

CHAPTER THREE: AFTERSHOCK ANALYSIS

A pertinent question seismologists struggle to answer is where an earthquake is most likely to occur and what are the driving mechanisms for coseismic motion. Answering these questions relies heavily on the characteristics of the geologic environment and the nature of the past seismicity in the region. Aftershock sequences can provide vital information regarding why and where these earthquakes may occur in the future. Earthquakes occur due to many environmental factors, such as strain accumulation and release, fluid pressure, or another earthquake (i.e., a triggered event) (Peng & Gomberg, 2010). Aftershock analysis can show migration paths of earthquakes over time (Ruhl et al., 2016). Detecting aftershocks enables researchers to determine what physical drivers are causing the earthquakes. Analyzing the temporal history of an earthquake can provide insight into faults and the amount of time expected between events. This is pertinent information needed to assess the seismic risk associated with a given area (Dieterich, 1994).

The most common methods used for aftershock detection require a high signal-to-noise ratio and/or a robust seismograph station network. Importantly, the inability to detect events with a low signal to noise ratio can limit tectonic interpretation, and thus there is an obvious motivation to use an automated detection method that is less sensitive to low signal-to-noise ratio. I first outline the traditional earthquake detection and picking process. I then compare this process to the recently developed EQT machine-learning

approach and highlight the differences in required signal-to-noise ratio. In the end of this chapter, I compare EQT's phase picking ability to hand-picked phases to validate using EQT phases for relocation. I note here that I have neglected a comparison of EQT and the other low signal-to-noise detection method called matched filtering. This is beyond the scope of this thesis. Instead, I focus on one machine-learning approach (EQT) and compare to the most common detection method.

3.1 Traditional Earthquake Detection and Phase Picking

A common earthquake detection method used by seismologists is the 'Short Term Average-Long Term Average ratio' (STA/LTA) trigger (Allen, 1982). This method is the most broadly accepted automated detection method used in earthquake detection far from an epicentral source (Trnkoczy, 2009). The method applies a specific picking threshold to a moving window amplitude ratio (i.e., the short-term average over the long-term average); if the amplitude of the ratio signal surpasses a given amplitude threshold, a picking trigger is turned on; once amplitudes decrease beneath a pre-set threshold, the trigger is turned off (Trnkoczy, 2009).

The time-period of data between the station trigger on and off is considered the earthquake time series on that station. This process is repeated over all stations in the network. Then, through either automated picking (traditionally not based on machine-learning) or hand picking, P- and S-wave arrival times are estimated (Di Stefano et al., 2006). The availability of large seismic datasets has pushed the envelope of automated detection algorithms; however, despite seismologist's best efforts, automatic trigger mechanisms have been relatively inefficient when compared to the trained eye of a seismologists.

3.2 Machine-Learning based Earthquake Detection and Phase Picking

EQT is a multi-task deep neural network that can be used for simultaneous earthquake detection and phase picking. This approach recognizes similarities in waveforms to an existing detected earthquake and uses this as a method to detect potential aftershocks (Mousavi et al., 2020). The process for identification can be broken down into two levels of self-attention, a global and local level. Each level helps the program capture and exploit dependencies between local (individual phases) and global (full waveform) features that are characteristic of an earthquake signal (Mousavi et al., 2020). The continuous data fed to the algorithm are three-component seismograms. The three-components consist of north-south, east-west, and vertical components that provide absolute ground displacement at the sensor.

EQT's event detection process relies on the visual characteristics of a seismic signal, specifically, the full waveform, and the P- and S-wave first arrivals. The algorithm is implemented in the Python language. The algorithm uses one deep encoder and three separate decoders; an event detector, a P-picker, and a S-picker (Mousavi et al., 2020). The attention mechanisms within this neural network are inspired by a human's visual attention, like how a seismologist would identify an earthquake signal by noticing a P-wave and an S-wave, with the P-wave arrival always before the S-wave. After analyzing each station, the signal characteristics are compared to the characteristics that were observed in a similar time window across multiple stations. When time windows have characteristics that look like earthquakes across multiple stations, an earthquake is detected. The algorithm was trained using the Stanford Earthquake Dataset (STEAD). The STEAD dataset is a large-scale global dataset of labeled earthquake and non-

earthquake signals. To train EQT, one million earthquake and 300,000 noise waveforms (including both ambient and cultural noise) were taken from approximately 2,600 seismic stations with epicentral distances up to 300 km. Many of the earthquake waveforms used in training are smaller than M2.5 and have been recorded within 100 km from the event epicenter (Mousavi et al., 2020).

The global training data set enables the neural network to become familiar with many different varieties of seismic signals, including noise. The goal of training in this way is to create a universal approach to seismic event detection and phase picking. Figure 3.1 shows all of the available stations used to acquire seismic data for training EQT. To test the program's ability to locate and pick earthquake waveforms and phase arrivals, EQT's high generalization ability was tested on five weeks of continuous data recorded during the 2000 Mw 6.6 Western Tottori, Japan earthquake (Figure 3.2). The Japan Meteorological Agency analyst picked 279,104 P- and S-wave arrival times on 57 stations; EQT was able to pick 401,556 P- and S-wave arrivals on 18 of those stations (Mousavi et al., 2020).
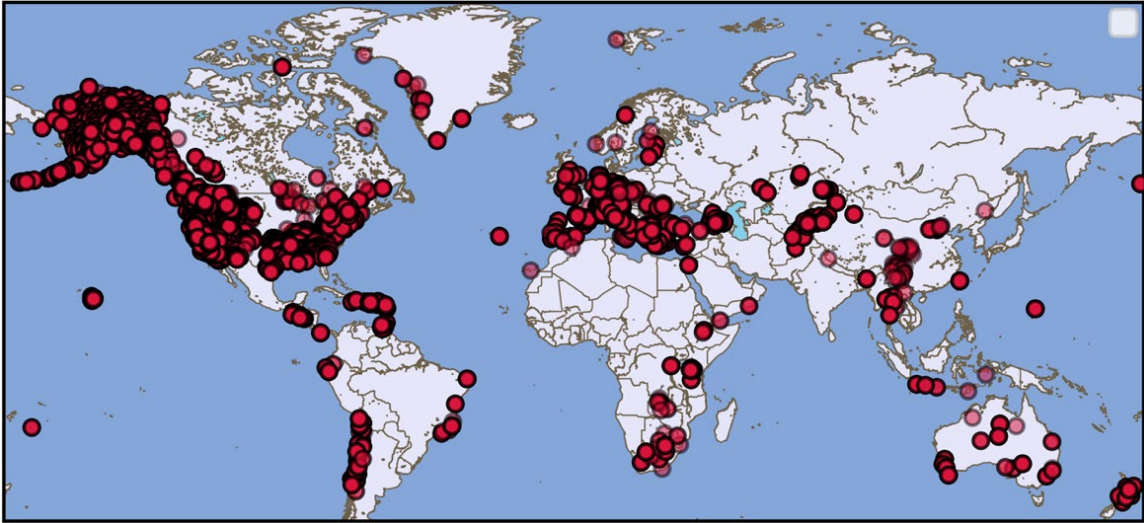
Figure 3.1   **Global map of earthquake station locations from the STEAD dataset used to train EQT from Mousavi et al. (2020).**
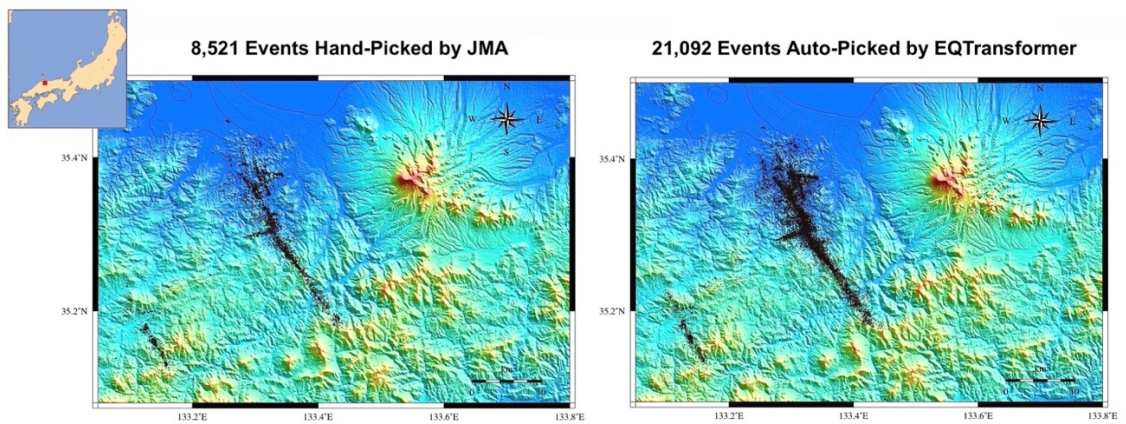
Figure 3.2   **Comparison of aftershocks picked by hand (left) to those picked by EQT (right) from Mousavi et al. (2020).**

3.3 Earthquake Transformer Validation

Rather than solely rely on the EQT creator's quality assurance tests described in Mousavi et al. (2020), I compared phase-picks using the EQT results for the Stanley aftershock sequence and our hand-picked events. Blaine Bockholt, Dylan Mikesell, Kristinia Rossavik, and I picked P- and S-wave arrivals for all aftershocks M>2.5 (U.S. Geological Survey, 2022b) using the Seisan program (Havskov and Ottemoller, 1999).

The catalog used both regional and local seismic stations, described in Chapter 4, consisting of approximately 2,000 hand-picked events. Using the bounding box parameters presented in Table B.1, we set the geographic area EQT could search for available station data. The minimum and maximum latitude and longitude bounds were set to the main shock location +/- 0.5 degree of latitude and longitude. In this way, we created a 1-degree x 1-degree (~110 km x 110 km) square from which to process seismic data for each aftershock sequence.

Once the geographic area is set, EQT needs to be parameterized for event detection and phase association. Figure 3.3 shows hand-picked events detected though identifying phase arrivals associated with the USGS catalog's recorded origin times and comparing them to the phase arrival times identified by EQT. EQT detected 94% of the events in the USGS catalog. For this 94%, I computed the P- and S-arrival time differences between our picks and the EQT picks. The mean P-wave arrival time difference was 0.0217 s and the mean S-wave arrival time difference was 0.0043 s. The mean absolute deviation (MAD) was the same, 0.08 s for both P- and S-wave arrivals, exploiting the algorithms picking consistency despite the usual difficulties associated with detecting the S-wave signal from within the overlapping P-wave (Figure 3.3). The results were promising in comparison to what was achieved by the USGS, but they were also reasonable when compared to other applications using EQT.

Mousavi et al. (2020) compared hand-picked phases to the EQT picks using the data from the JMA data set. Their results provided a mean P-and S-wave arrival time difference of 0.01 seconds for 279,104 earthquakes. The phase arrival differences using the Stanley events were slightly greater for the P-wave arrivals, but less than the mean

arrival time difference for the S-wave arrivals (Mousavi et al., 2020). The standard

deviation obtained using the Stanley phases, P-wave σ = 0.19 s and S-wave σ = 0.16 s,

were slightly greater than the results obtained by Mousavi et al. (2020), P-wave σ = 0.08

s and S-wave σ = 0.07 s. Relative to the size of each data set the σ is low and did not

deviate drastically from the mean arrival time difference in either study. Thus, EQT is

capable of being used in other geologic settings and therefore the neural network was

assumed to not need further training.
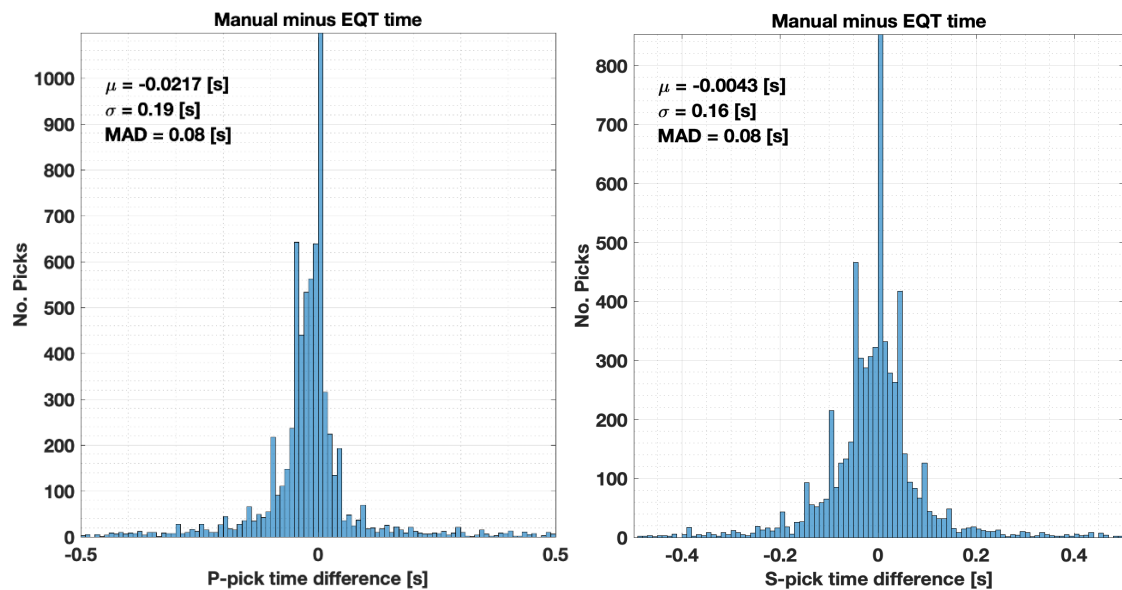
Figure 3.3 **P-wave pick time difference (left) and S-wave pick time difference (right). Presented are the average time difference (μ), the standard deviation (σ), and the mean absolute deviation (MAD).**

CHAPTER FOUR: APPLICATION OF EQT TO THREE AFTERSHOCK

SEQUENCES

4.1 The Local Seismic Networks

Before implementing a traditional earthquake detection method, or alternative

method like EQT, a seismic network must be deployed. The seismic networks for each

sequence were comprised of both regional, permanently deployed broadband

seismometers, and local networks consisting of temporarily deployed broadband

seismometers less than 50 km from each epicentral region (Pang et al, 2018; Koper et al.,

2018; Liberty et al., 2021). The station geometry for each sequence varied and this

variable is reflected in each sequence's aftershock catalog, which I will explain later in

Chapter 5.

Although local networks are known to constrain seismic event locations and have

lower travel time residual errors, waveforms from local station data can be hard to pick

by hand. The trouble arises when events occur in a small window of time relative to other

events, causing them to overlap in the recorded signal. The stacking of signals inherently

makes the phases difficult to detect visually, even after STA/LTA trigger detection

(Beroza, 1995). Detection algorithms like EQT avoid this issue by using waveform

matching to detect events and locate phases across multiple stations (Mousavi et al.,

2020). In Figure 4.1 the local seismic arrays surrounding each sequence and the available

regional network that was used to construct the USGS catalogs are shown.
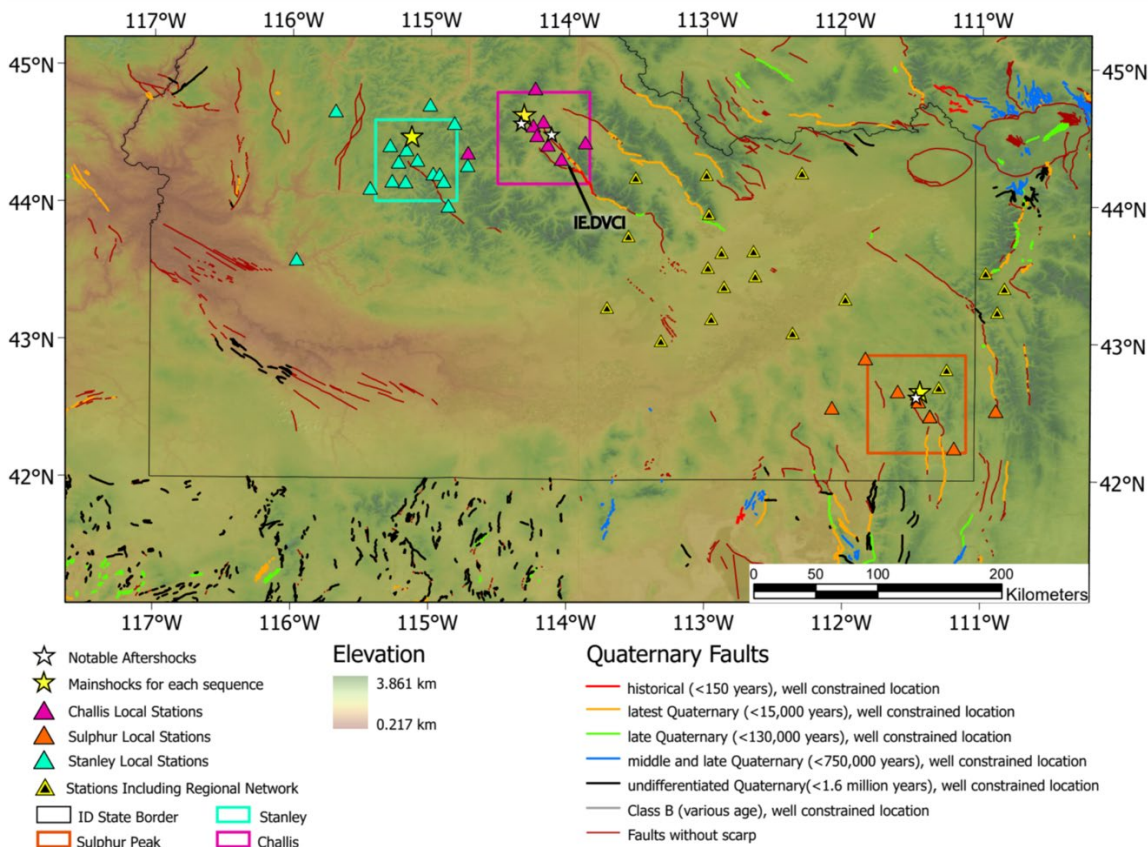
Figure 4.1   Regional Map with temporary networks for each sequence and regional network along with the INL network (e.g., U.S. Geological Survey, 2022b). The station IE.DVCI corresponds to the only local station left to record seismicity during the second rupture of the Challis Sequence in 2015.

4.1.1 The Stanley Seismic Network

A Boise State team worked with the U.S. Geological Survey and Idaho Geological Survey to deploy 16 temporary broadband plus strong-motion seismometers near the epicentral region of the Stanley mainshock (Network XP and GS; stations: FOX, BANN, SAC, WARM, ATL, DDR, EPIC, IRON, SUNB, TRAP, TRP2, RDFL, TWRS, PETL, MFRD, and ID11) (Liberty et al., 2021). These stations, along with the regional network, Figure 4.1, provided local waveforms to generate an improved aftershock catalog. The temporary stations were deployed within the first two weeks following the mainshock and retrieved between October 28 and December 1, 2020. The analysis in this

thesis covers the time span from April 1 through December 31, 2020. Due to the changing network coverage, I study the influence of changing the local station geometry on the EQT results.

4.1.2 The Sulphur Peak Seismic Network

The Sulphur Peak sequence was recorded both regionally and locally using a temporary network of six broadband seismometers plus strong-motion (Network GS; stations ID [05-10]) and two strong-motion accelerometers (Network UU; stations: ASI4 and ASI5). These stations were deployed within 4 to 10 days of the mainshock (Koper et al., 2018). The six GS stations were deployed starting on September 9, 2017 and demobilized in the end of October 2017, while the two UU stations remained active, although station ASI5 was moved 90 m and renamed ASI6. Figure 4.1 shows the current position of station ASI6 and not the AS15 position (Koper et al., 2018).

4.1.3 The Challis Seismic Network

The Challis sequence was recorded both regionally and locally following the first mainshock in April of 2014 (Pang et al., 2018). The local network was deployed as a combined effort between the University of Utah, Montana Bureau of Mines and Geology, INL, IGS, and USGS. The temporary network consisted of eight three-channel-component broadband seismometers deployed April 4, 2014 and retrieved at the end of October 2014 (Networks GS, IE, and UU; stations ID01, ID02, ID03, ID04, DVCI, ASI1, ASI2, and ASI3). One local station, station DVCI, deployed by INL under the network code IE, became a permanent station and recorded the second sequence that initiated in January of 2015. The lack of local coverage for the aftershocks that followed the January 2015 sequence is reflected in EQT's detected phases and interpretive results.

4.2 Associated Velocity Models

The standard velocity model used in earthquake locations is the AK-135f model (Montagner & Kennett, 1996), which I obtained from the IRIS Data Management Center. The USGS uses this model for their earthquake hypocenter location estimation. I compare this velocity model to three other velocity models by examining hypocenter inversion travel time residuals for every identified event. The AK-135f model, the two previous regional models used in Koper et al. (2018) and Pang et al. (2018) papers, and my own velocity model derived from smoothing AK-135f are listed in tables D1-4 in Appendix D.

4.2.1. North of the Snake River Plain

For the Stanley and Challis sequences, I use a smoothed AK-135f model for hypocenter determination (Table D.2). In this model, the P- and S-wave velocities gradually increase with depth. I refer to this model as the *Gradient model*. In the results section, I compare the Challis regional velocity model used by Pang et al. (2018) to my Gradient model. Their regional model was created from a geologic interpretation of the 1983 Borah Peak earthquake rupture zone (Shemeta, 1989). Based on hypocenter results, I use my new model for both the Challis and Stanley sequences, which lie to the north of the Snake River Plain. To see the results using the Challis model reference Figure E.7 in Appendix E. Considering only three models are used in my results and interpretation, only those three models are compared in Figure 4.2; however, all four velocity models are listed in the Appendix D.

4.2.2. South of the Snake River Plain

The regional velocity model for the Sulphur Peak sequence is derived from previous research by Brumbaugh et al. (2001), who used this model in the relocation of hypocenter events following the Draney Peak earthquake. The Brumbaugh model (Table D.4) was also used by Koper et al. (2018). I tested the Gradient model for the Sulphur Peak sequence, but I chose to use the Brumbaugh model for direct comparison of my results with the results of Koper et al. (2018). This comparison can be found in Chapter 5. Thus, south of the Snake River Plain I use the Brumbaugh model, which is distinctly different from the model I use for the sequences north of the Snake River Plain. Figure 4.2 shows the P- and S-wave velocities for the AK-135f, Gradient (i.e., smoothed AK-135f), and Brumbaugh models. The main velocity differences are in the upper 5km. The Gradient model has faster velocities than the Brumbaugh model in the upper 5km, while below this Brumbaugh is slightly faster down to 30km depth. I note that the velocity models used in this thesis are solely based on a comparison of the residual error for the three models. A more accurate velocity model (e.g., 2-D or 3-D) could further improve aftershock hypocenter estimates.
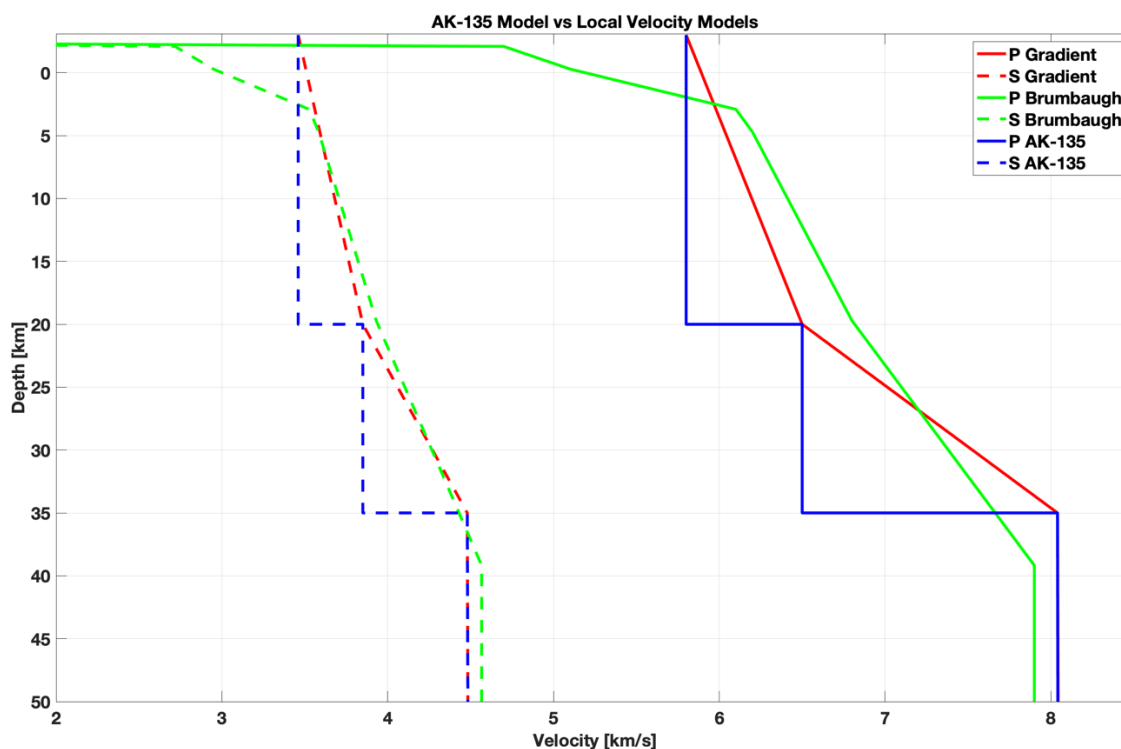
Figure 4.2 **Brumbaugh, AK-135f, and the Gradient (i.e., smoothed AK-135f) velocity models used for hypocenter estimation in Hypoinverse.**

4.3 Hypocenter Estimations through Hypoinverse

Using the velocity models described in the previous sections, I locate each aftershock with the program Hypoinverse (Klein, 2014). I use Hypoinverse for hypocenter estimation because it relies on a 1-D velocity model and simplifies the comparison of EQT to the results of Pang et al. (2018) and Koper et al. (2018), whose results were also obtained using 1-D local velocity models. Hypoinverse minimizes the arrival times between phase arrivals that are predicted and those that were measured at multiple stations distributed over an area. Using 1-D P-and S-wave velocity models to predict the travel times, the depth, epicenter, and origin time (i.e., the hypocenter) of each aftershock is determined based on which combination of these parameters provides the

minimum error between predicted and observed arrival times. Thus, the velocity model plays an important role in the travel time prediction process.

In addition to the hypocenter parameters, Hypoinverse provides a quality parameter obtained from the residual travel time errors and the event-to-station distance (Klein, 2014). Using all the hypocenters for each sequence, I compare Hypoinverse quality ratings to their corresponding residual errors. The aim of this exercise is to determine whether the Hypoinverse quality rating is the best parameter to determine which EQT picks provide useful earthquake hypocenters. Given that the EQT process is fully automated, with only a few parameters that can be changed, it is important to identify ways to quality control (QC) the final hypocenter estimates. The quality rating from Hypoinverse is simply one approach. I determine my own approach in the next section.

4.3.1 Producing a High-Quality Catalog

The quality rating determined by Hypoinverse consists of A-, B-, C-, and D-type events. The A-type events are located with the highest certainty. The D-type events are the poorly located hypocenters with the highest spatial uncertainty. Hypoinverse uses seven parameters to assign quality to a hypocenter estimate: root-mean-squared (RMS) travel time residual, ERH (horizontal location error), ERZ (vertical location error), NWR number of weighted stations reading phases, MAXGAP (maximum angular gap in degrees between azimuthally adjacent stations), the earthquake depth uncertainty, and the minimum distance to the closest station. Using these parameters, Hypoinverse applies a quality rating that is an average of two weighting parameters (Klein, 2014). The first quality rating is based on errors and goodness of fit. The letter next to the range of values

below represents the level of quality that Hypoinverse associates with those values, A- being the best, D- being the worst.

A. RMS < 0.15 sec and ERH ≤ 1.0 km and ERZ ≤ 2.0 km

B. RMS <0.30 sec and ERH ≤ 2.5 km and ERZ ≤ 5.0 km

C. RMS < 0.50 sec and ERH ≤ 5.0 km

D. Greater than above

The second quality rating is based on station geometry:

A. NWR ≥ 6 and MAXGAP ≤ 90 and either DMIN ≤ DEPTH or DMIN ≤5.0

B. NWR ≥ 6 and MAXGAP ≤ 135 and either DMIN ≤ 2*DEPTH or DMIN ≤10

C. NWR ≥ 6 and MAXGAP ≤ 180 and DMIN ≤ 50

D. Greater than above

The distance from the event to the nearest station is weighted using a kriging approach. The ideal-distance weighting scheme reduces the weight of the distant stations when an event is detected within the interior of a seismic network (Klein, 2014). The Hypoinverse distance weighting function is 1.0 for near stations and 0.0 for far stations; for stations in-between, the weighting follows a cosine taper. Figures 4.3-4.5 display the spatial and temporal uncertainties for each sequence's hypocenters, Stanley, Sulphur Peak, and Challis, respectively, colored by Hypoinverse event type. The velocity model used in all figures is the Gradient model.
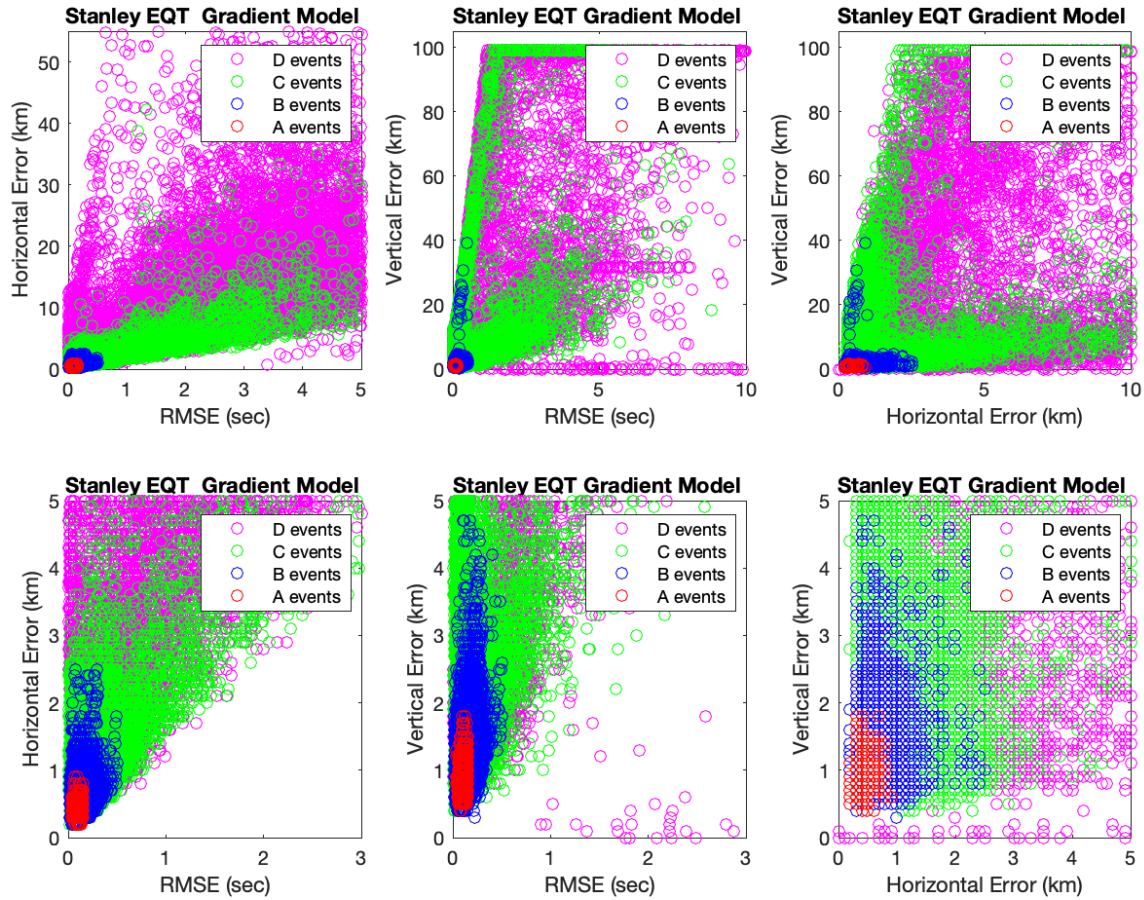
Figure 4.3   The distribution of A-, B-, C-, and D-events determined by Hypoinverse for Stanley; bottom panels are zoomed versions of the top panels. The plots show the relationship between ERZ, ERH and RMS residual error for each event type.
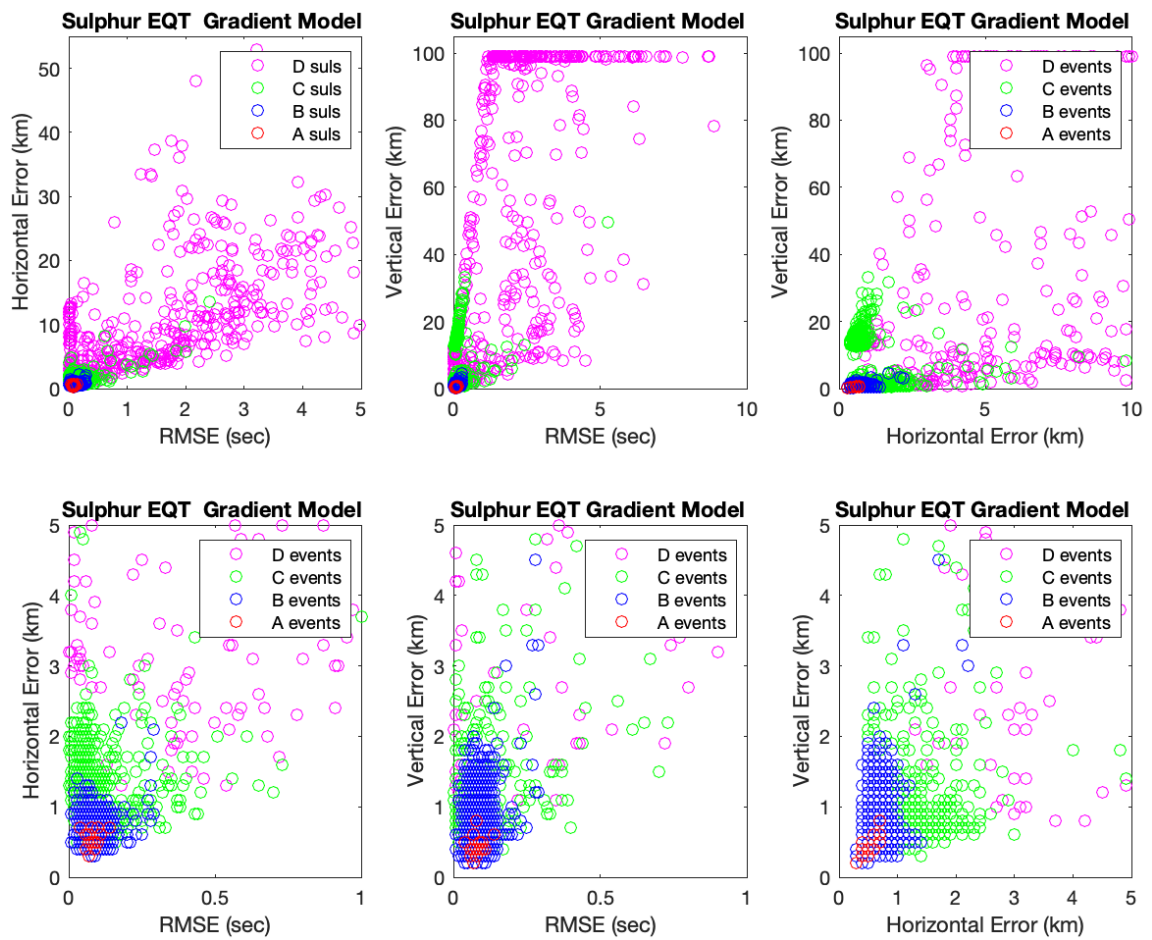
Figure 4.4   The distribution of A-, B-, C-, and D-events determined by Hypoinverse for Sulphur Peak; bottom panels are zoomed versions of the top panels. The plots show the relationship between ERZ, ERH and RMS residual error for each event type.
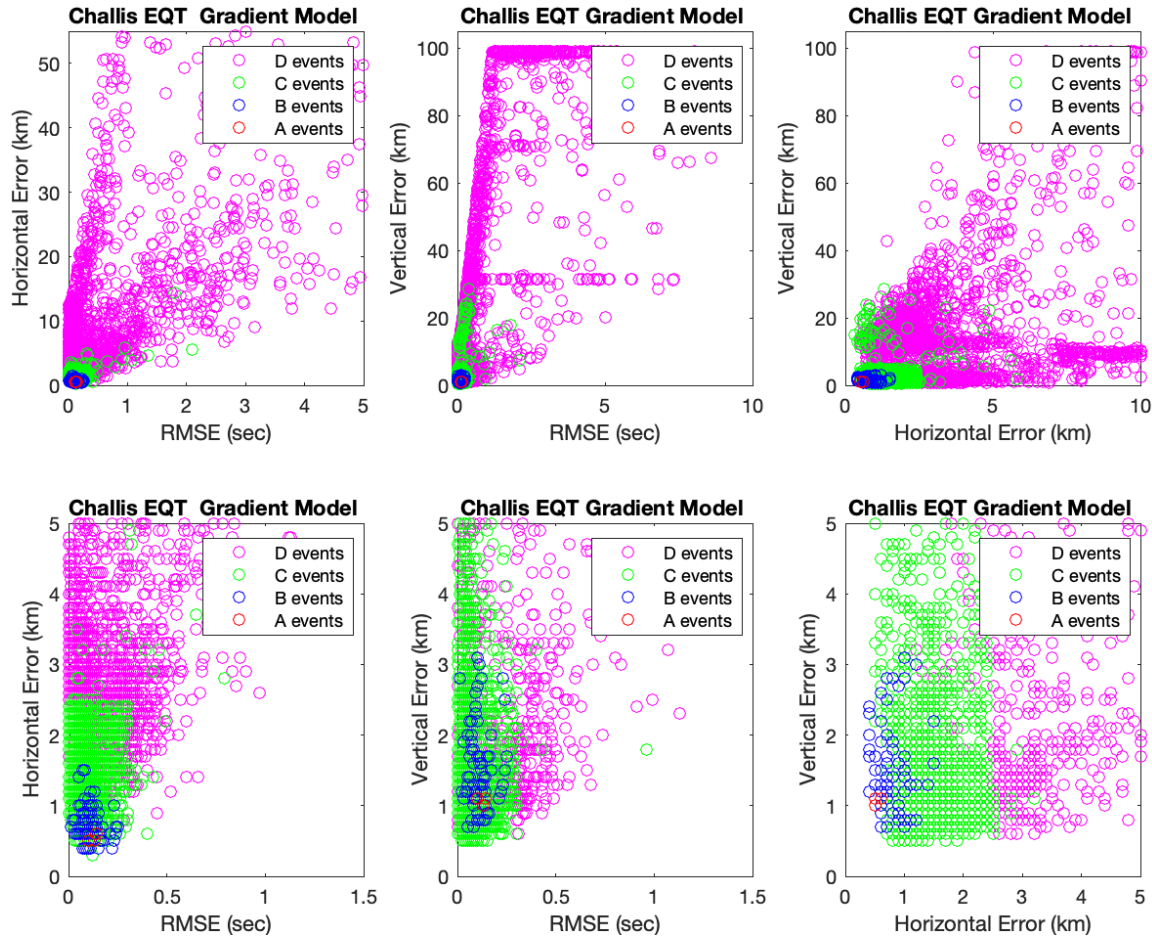
Figure 4.5   **The distribution of A-, B-, C-, and D-events determined by Hypoinverse for Challis; bottom panels are zoomed versions of the top panels. The plots show the relationship between ERZ, ERH and RMS residual error for each event type.**

Based on analysis of event type to the different hypocenter error estimates, it is clear that the station distance parameter used in evaluating location quality had assigned poor quality ratings to reliable earthquake locations. Figures 4.3 through 4.5 show that all event types can have both high and low residual errors. Many of the C- and D-type events have high residual errors and can therefore be neglected; however, not all these poorly rated events have unreliable hypocenter estimations. Many of these events had quite small error estimates and travel time residuals (lower panels in Figures 4.3-4.5). When

considering their spatial locations, they map to the same regions as A- and B-type events, often with the same magnitude of error.

The waveforms and travel time picks used to produce my final aftershock catalogs are determined using only the spatial error and depth. As observed in Figures 4.3-4.5, many C- and D-type events have horizontal and vertical errors less than 5 km. In addition, many C- and D-type events have travel time residuals less than 1 s. Thus, any event that occurred at a depth greater than 20 km or an ERZ or ERH ≥5 km was not added to the final aftershock catalogs. This is because 20 km is deeper than the presumed seismogenic zone for south Idaho (Anders et al., 1989; Doser & Smith, 1985) and because the spatial errors were larger than the distances, we wanted to asses in the spatial patterns of aftershock seismicity for each sequence. Using these *high-quality* hypocenters, we assess the EQT location and compare them to the results of Pang et al. (2018) and Koper at al. (2018).

CHAPTER FIVE: MACHINE-LEARNING RESULTS

5.1 EQT Results and Comparisons

To assess the EQT event detection and phase picking approach, I search each unfiltered EQT catalog for matching events in the USGS catalog. Events are considered a match if their origin time difference is less than 10 seconds. If multiple EQT events fall within these 10 second times differences, I take the EQT event closest to the USGS origin time. This is done to determine if EQT identifies and picks events that were independently identified and hand-picked by a USGS seismologist/analyst. Additionally, it allows me to assign earthquake magnitude to corresponding EQT aftershocks.

5.1.1. Stanley Results

The first thing to consider is the event identification using EQT. Figure 5.1 shows a significant drop in number of EQT detected events at the end of October, indicated by the black line. The drop in detected events coincides with the removal of the local seismic stations. We see that this is not the case for the USGS catalog. This is likely due to the USGS seismic-analyst picking events not detected on at least three seismic stations, therefore unable to be identified by EQT.

The next thing to consider is how well EQT identifies events, specifically those picked by a seismic-analyst. Comparing the USGS catalog to my complete EQT catalog, I note that approximately 89% of the USGS aftershocks are identified within the 74,670 event EQT catalog. From the high percentage of matched events, I confirm that EQT

does identify Stanley aftershocks and that the Gradient model does not measurably influence the arrival times of events located using the AK-135f model. Of the 113 USGS events that were not detected by EQT, I speculate that this could have resulted from a poorly picked phase within the USGS catalog (or EQT) resulting in an origin time difference greater than my 10 s threshold.
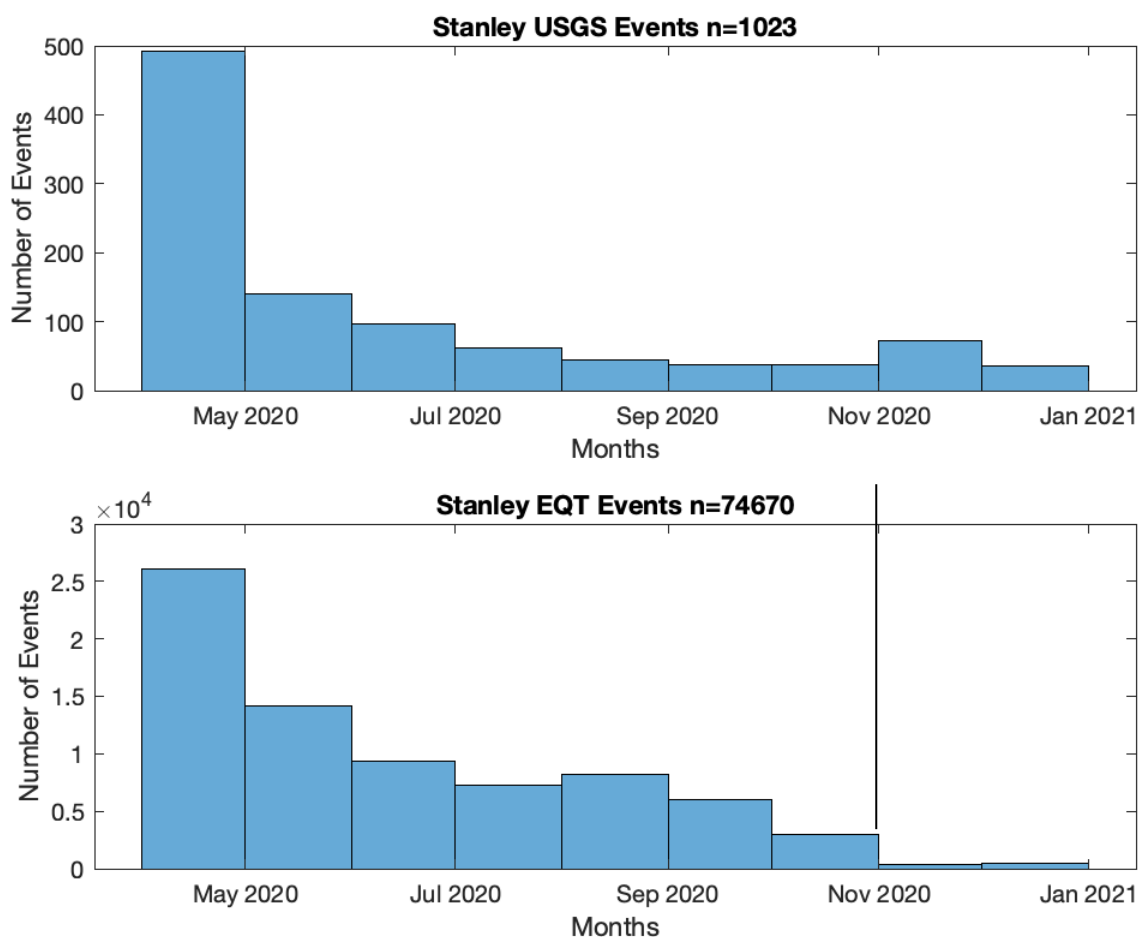
Figure 5.1   Number of detected Stanley aftershocks binned by month from the USGS (top) and EQT (bottom) catalogs spanning from April through December 2020. Here "n" equals total number of detected aftershocks. The solid black line represents local station removal in the lower plot near November 2022.

I next compare the high-quality EQT catalog (i.e., ≤5 km ERZ and ERH, <20 km depth) created with the Gradient model to the same EQT events obtained using the AK-135f velocity model. EQT provided 52,125 high-quality events using the Gradient

velocity model, but only 2,265 events when using the AK-135f model to locate

hypocenters using EQT picks. In my high-quality EQT catalog, 87% of all aftershocks

had an RMSE of less than 0.2 s compared to the 0.7 s returned by the AK-135f model.

Thus, I interpret the discrepancy as Hypoinverse being unable to find accurate

hypocenters using the AK-135f model due to this model not representing the 1-D

subsurface structure in the Stanley area. Using the Gradient model, all the spatial and

temporal residuals except for the standard deviation of the depth was reduced compared

to the AK-135f velocity model; thus, another indicator the Gradient model likely matches

the true subsurface more closely. The hypocenter error statistics for each velocity model

are presented in Table 5.1. It is clear that the Gradient model is superior to AK-135f

based on these results.

Table 5.1   The Stanley residual errors for the Gradient and AK-135f velocity models using EQT picks.

Total number of EQT Phase Picks 74672	Gradient Model	AK-135f Model
Number of Located Events	52125	2265
RMSE (s)	0.16	0.7
RMSE Std. Deviation (s)	0.85	3.6
Average Depth (km)	9.6	5

The Gradient model provided the lowest residual errors compared to the other

velocity models that I tested, but this is only one factor for the high number of detected

events. Figure 5.2 shows that average ERZ and ERH increased when fewer local stations

were deployed. These low deployment windows include the three weeks after the main

shock on March 31, 2020, and the months of November and December 2020. The low residual errors associated with EQT's detected events is strongly influenced by the availability of local stations and seismic network geometry. The local network allows EQT to make phase picks near the epicentral region of interest, thus diminishing the ERZ and ERH associated with events located farther away from a seismic station. Another way to say this is that the local stations provide a better constraint on the hypocenter. This is in part because these local stations are less influenced by incorrect velocity models compared to regional stations where the waves (i.e., P and S) have traversed a much larger distance.

Figure 5.2 **The change in average vertical (ERZ) and horizontal (ERH) error for the Stanley sequence through time (left axis). Station count used for EQT picks through time on the right axis.**

Finally, earthquakes are typically constrained to the brittle portion of Earth's crust. My catalog shows a mean aftershock depth of 9.6 km below sea level (Figure 5.3). I note that 92% of all aftershocks lie between 3 km and 15 km depth. The depth distribution shown below suggests that the maximum depth of the seismogenic zone is about 15 km below sea level.
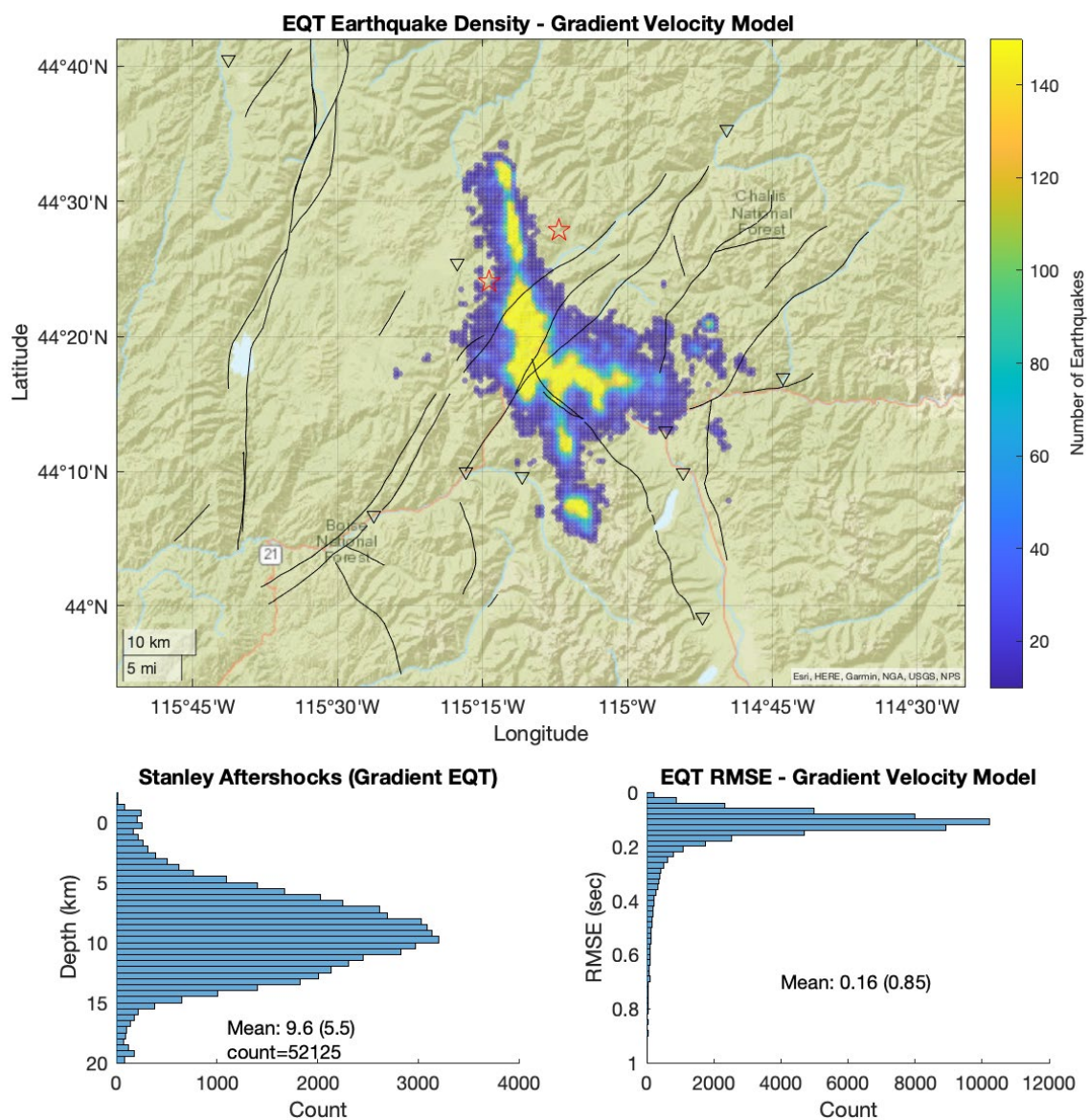
Figure 5.3 **Earthquake density map for Stanley using the Gradient model. The black lines are the TCFS from Lewis et al. (2012). The northern most star is the USGS location and the southernmost star is the Montana Bureau of Mines and Geology location (e.g., U.S Geological Survey, 2022b). The density map shows events binned in 0.5 x 0.5 km horizontal bins. The lower left panel shows the distribution of depths with the mean depth (standard deviation) and total number of events. The lower right shows the travel time root mean squared error with the mean (standard deviation).**

5.1.2 Sulphur Peak Results

The Sulphur Peak aftershock catalog derived from EQT and the Brumbaugh velocity model match only ~53% of the 551 USGS aftershocks identified between September 9, 2017 and October 28, 2017. The bottom panel of Figure 5.4 shows an initial gap in EQT detected events in early September. This is because the temporary network was not deployed until approximately a week after the mainshock. In addition, the spatial uncertainties presented in Figure 5.5 reflect this lack of station coverage, showing that the average ERZ and ERH are greatest at the start of the sequence.
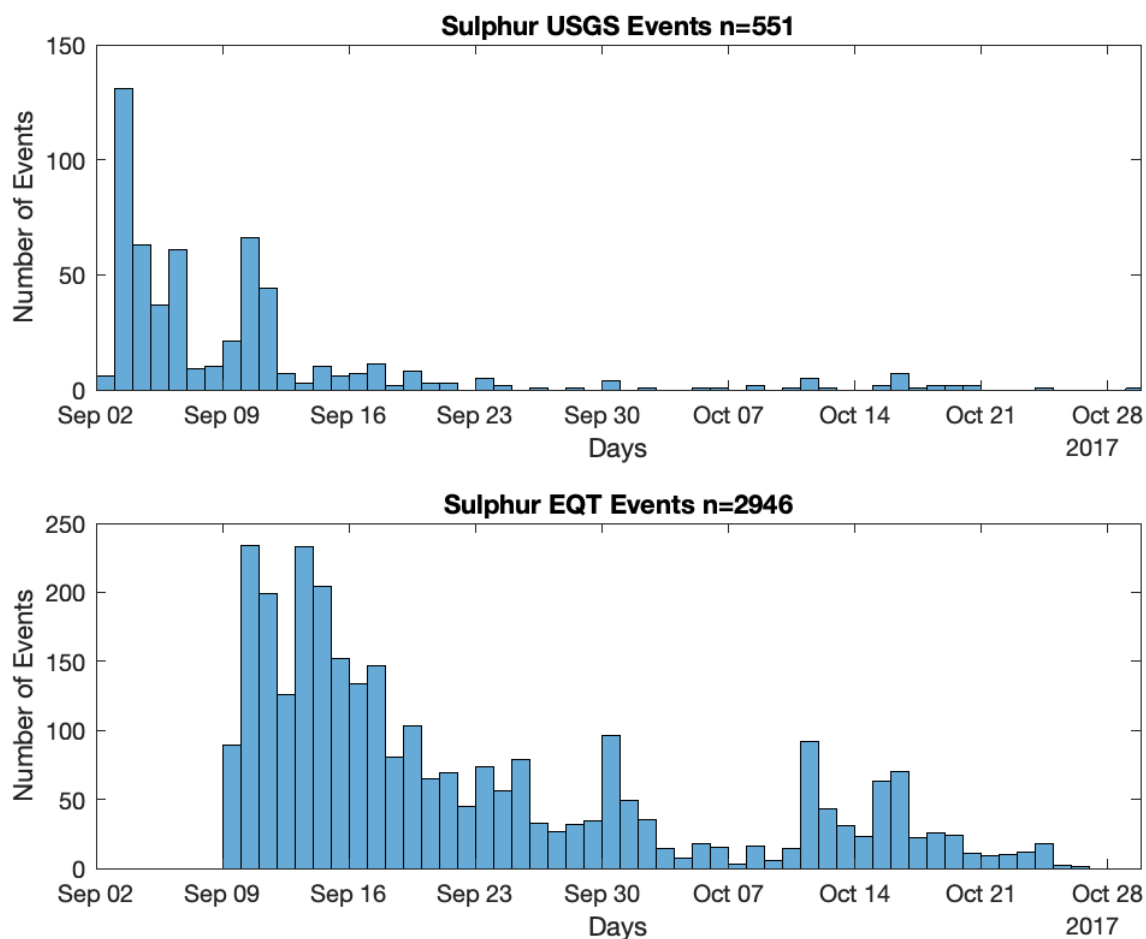
Figure 5.4 **Number of detected events for USGS (top) and EQT (bottom) binned by day for the Sulphur Peak sequence; "n" equals total number of events in each catalog.**

I compare the EQT residual errors with locations derived using the Brumbaugh, Gradient, and AK-135f velocity models. Using the Brumbaugh velocity model, I obtain 2,170 aftershocks. With the Gradient model, I obtain 2,336 aftershocks. Using the AK-135f model, only three aftershocks are located. The errors for the Gradient model were the lowest and returned more high-quality hypocenters (i.e., ERH ≤5 km and ERZ ≤5 km). Despite the low residual error, the depth distribution was greater than the reported depths published by Koper et al. (2018). The results suggests that the Sulphur Peak aftershock sequence may be improved with a different velocity model. The scope of my

research involves testing the quality of EQT picks in conjunction with previous published results. Therefore, to assess the measurable quality of EQT, I opted to use the published velocity model rather than the Gradient model. The residual errors for all velocity models are presented in Table 5.2.

Table 5.2   The Sulphur Peak residual errors for the Brumbaugh, Gradient, and AK-135f velocity models.

Total number of EQT Phase Picks 2946	Brumbaugh Model	Gradient Model	AK-135f Model
Number of Events	2170	2336	3
RMSE (s)	0.09	0.08	2.4
RMSE Std. Deviation (s)	0.07	0.06	0.1
Average Depth (km)	5.4	9	5.8

Figure 5.5 shows that at the initial start of the Sulphur Peak aftershock sequence, the average ERZ and ERH for estimated hypocenters were at their maximum. In the third week of the sequence, another local station was deployed and the ERZ and ERH decreased further. ERH seems to slowly increase and then decrease over time, whereas ERZ remains consistent once all eight temporary stations are deployed. Prior to the deployment of temporary stations EQT is incapable of detecting events, which accounts for the lack of ERZ and ERH prior to September 9, 2017, in Figure 5.5.
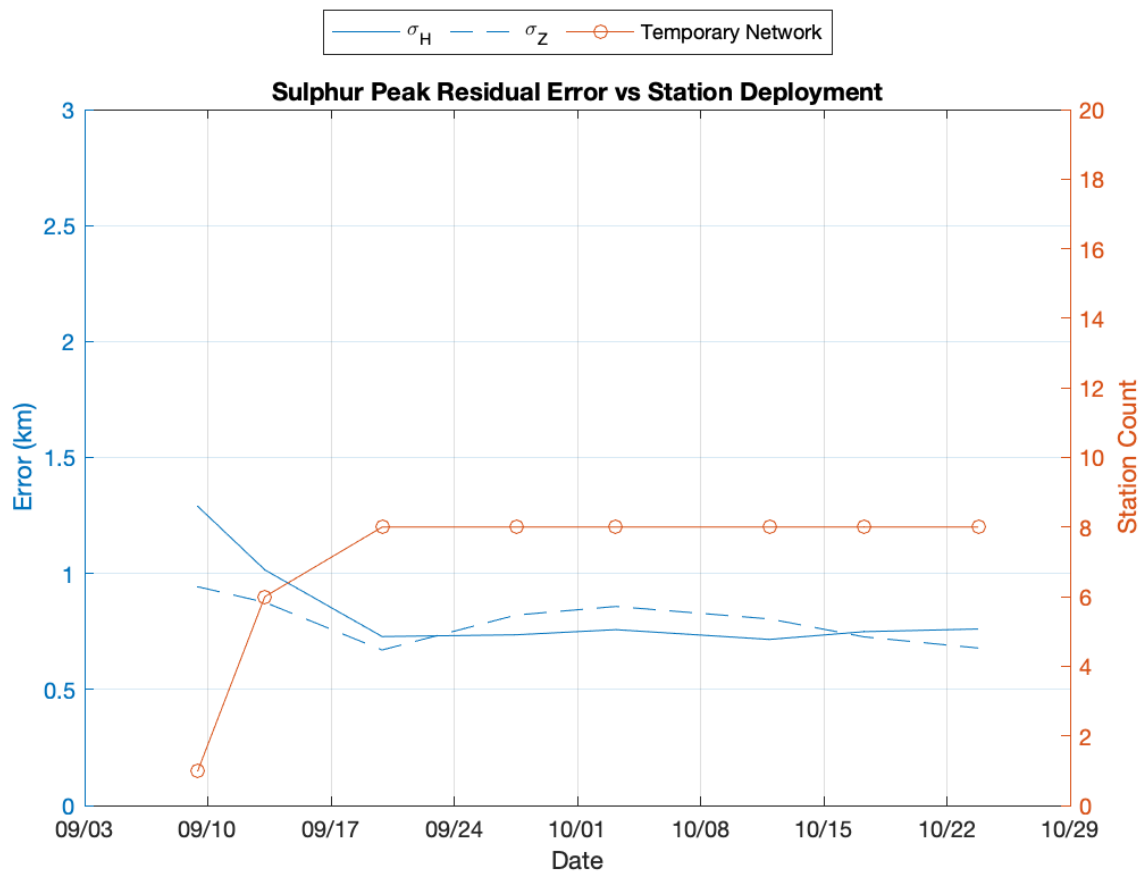
Figure 5.5   The change in average vertical (ERZ) and horizontal (ERH) error for the Sulphur Peak sequence through time (left axis). Local station count used for EQT picks through time on the right axis.
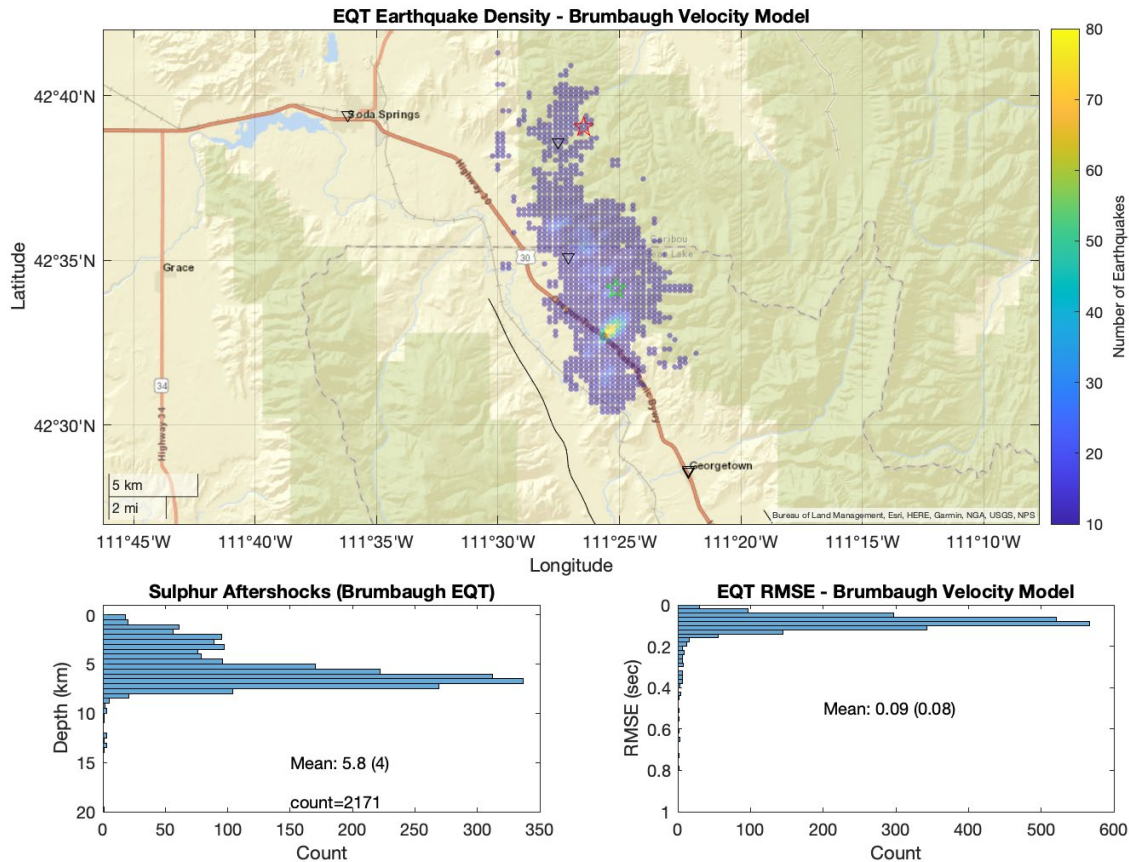
Figure 5.6 **Earthquake density map for Sulphur Peak using the Brumbaugh velocity model (Brumbaugh, 2001). The red star is the mainshock location and the green star represents the town of Soda Springs, ID. The black line is the EBLF from the USGS quaternary faults and folds database (U.S. Geological Survey, 2022c). The density map shows events binned in 0.25 x 0.25 km horizontal bins. The lower left panel shows the distribution of depths with the mean depth (standard deviation) and total number of events. The lower right panel shows the travel time root mean squared error with the mean (standard deviation).**

The Sulphur Peak aftershock sequence was characterized as being highly energetic and not entirely dominated by tectonic processes (Koper et al., 2018). The total number of high-quality aftershocks was 2,170 using the Brumbaugh model and 2,336 using the Gradient model. The observed mainshock-aftershock sequence using either velocity model does not follow the relationship of aftershock magnitude expected from Båth's Law (Båth, 1965). The depth distribution of events for Sulphur Peak was measurably shallower compared to the Stanley sequence depths shown on the depth

distribution plots (Figure 5.6 for Sulphur Peak and Figure 5.3 for Stanley). The mean travel time RMSE for Sulphur Peak events was 0.09 seconds (Figure 5.6). The high-quality events outline a N10W trending aftershock alignment (Figure 5.6) with a concentration of events south of Soda Springs (green star on map). This is a similar pattern as shown in Koper et al. (2018). We do not interpret our hypocenter results beyond this brief comparison. It appears that the EQT results are consistent with the published results of Koper et al. (2018). It is possible that future work here could be done to better understand the shallow seismicity, but this is beyond the scope of this thesis.

5.1.3 Challis Results

Despite a sparse array of temporary seismometers following the initiation of the second Challis 2015 mainshock, I use EQT and the Gradient model to identify a localized concentration of aftershocks to the south of the 2014 main shock (Figure 5.7). Figure 5.8 shows the monthly distribution of aftershocks detected by EQT using the Gradient model compared to temporal distribution of aftershocks in the USGS catalog. Comparing USGS and EQT origin times, I note that 161of the 189 USGS cataloged events were detected by EQT.

The two observed peaks in aftershock densities (Figure 5.8) indicate two distinct sequences starting in April 2014 and January 2015, respectively (Pang et al., 2018). Another interesting characteristic of this sequence is that fewer number of aftershocks followed the second mainshock. I identify 2,095 aftershocks between April through December, 2014 and 737 aftershocks following the second mainshock on January 1, 2015. Between April 14, 2014, and December 31, 2014, I note a reduction of seismicity with time as would be expect with any earthquake. However, the second mainshock is

followed by a rather abrupt decrease in aftershocks after one month. Pang et al. (2018) observed an active period of seismicity following the January 2015 mainshock, but this is not observed using EQT. I suspect this result reflects the poor station availability and inability of EQT to detect events without a dense array of seismometers and not related to tectonic processes. While there was one local station available at this time, the minimum requirement for EQT to consider an event an earthquake is that it must be detected on three different (local) stations. Therefore, as event magnitude decreased with time, the likelihood of events being detected using the regional network decreased as their amplitudes likely did not exceed background noise levels and the difference in arrival times may have been too great, i.e., >10 seconds, to be considered the same earthquake.
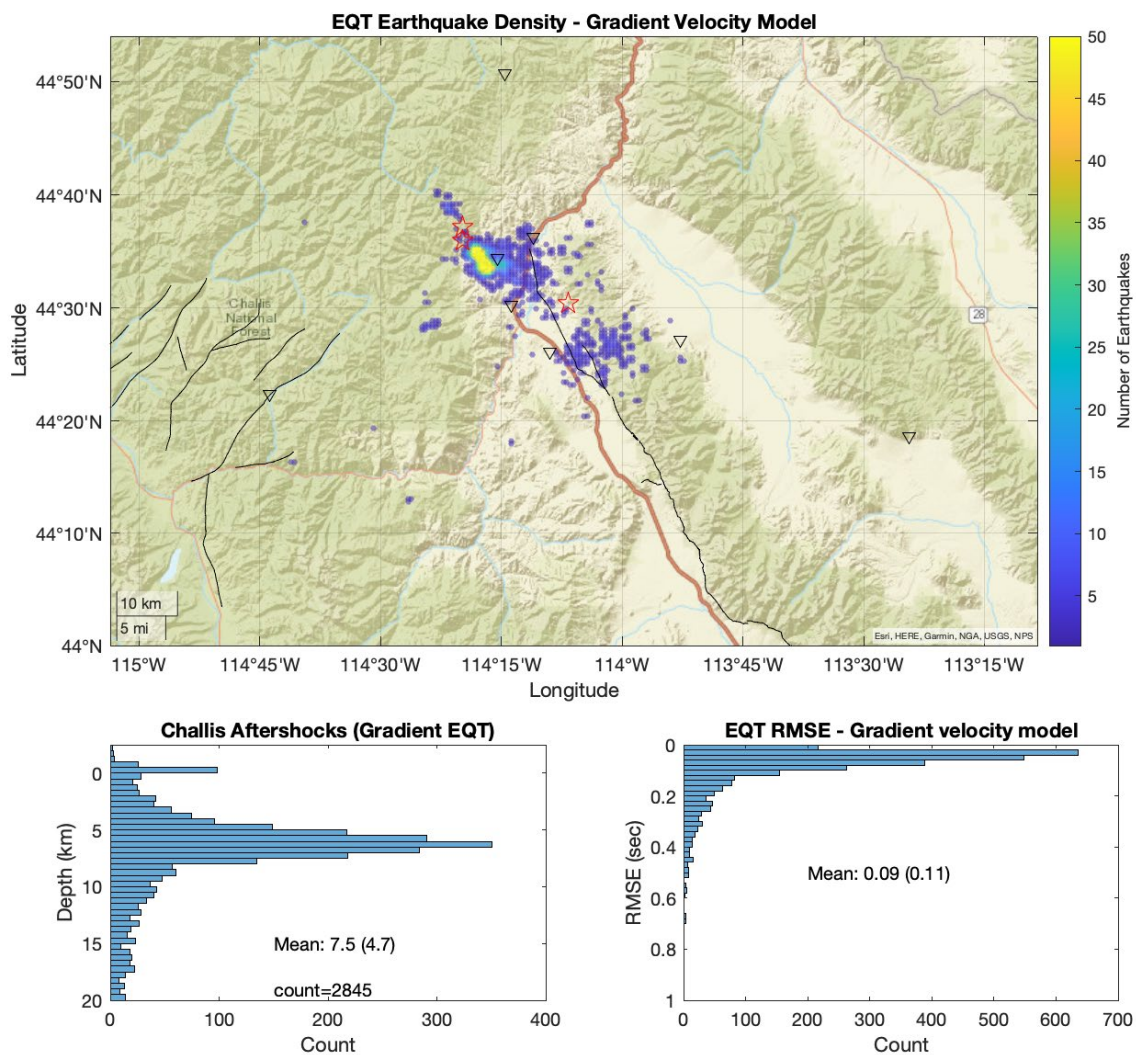
Figure 5.7   Earthquake density map for Challis sequence using the Gradient model. The black lines to the west are the TCFS from Lewis et al., (2012) and the black line to the east intersecting the southern portion of seismicity is the Lost River fault (U.S. Geological Survey, 2022c). The two red-stars to the north-west are the first two M>4 events that occurred in April 2014, and the star to the south is the M5.1 event that occurred on January 1, 2015.The density map shows events binned in 0.5 x 0.5 km horizontal bins. The lower left panel shows the distribution of depths with the mean depth (standard deviation) and total number of events. The lower right panel shows the travel time root-mean-squared error with the mean (standard deviation).
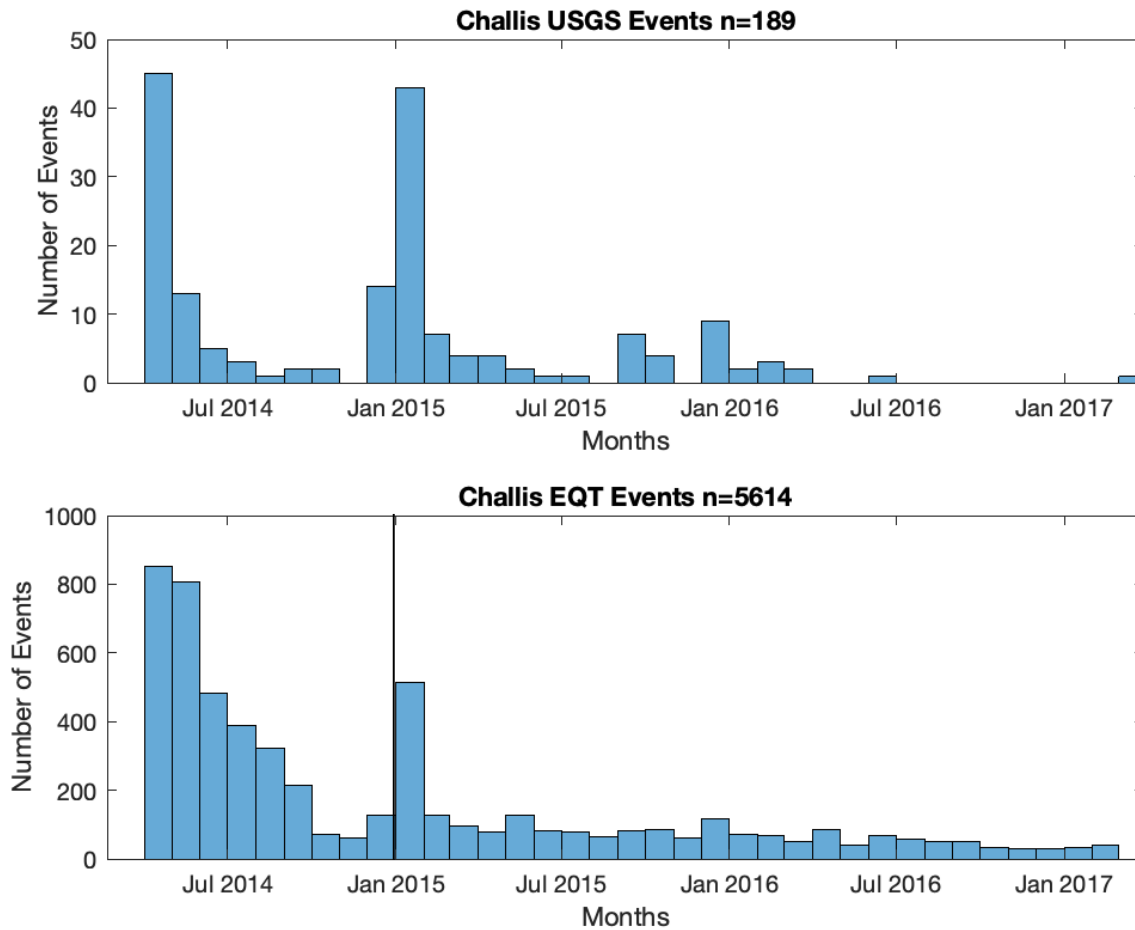
Figure 5.8   Number of detected events for USGS (top) versus EQT (bottom) binned by month starting in April 2014 and ending in March 2017 for the Challis Sequence. Here "n" equals total number of detected events. The black line in the lower plot represents the start of the second sequence on January 1, 2015.

Using the high-quality (i.e., ERZ ≤5 km and ERH ≤5 km) events, I compare the

residual error of EQT detected events located using the local Challis (Shemeta, 1989),

Gradient, and AK-135f velocity models. I located 2,401 hypocenters using the Challis

model, 2,845 using the Gradient model, and 852 using the AK-135f model. All the spatial

and temporal residuals using both the Gradient model and Challis model were lower than

what was obtained using the AK-135f model. The Gradient velocity model not only

outperformed AK-135f, but also the local Challis velocity model used by Pang et al.

(2018). The residual error statistics are presented in Table 5.3.

Table 5.3   The Challis residual errors for the Challis (local), Gradient, and AK-135f velocity models.

Total number of EQT Phase Picks	Challis Model	Gradient	AK-135f
5614		Model	Model
Number of Events	2401	2845	852
RMSE (s)	0.23	0.09	0.18
RMSE Std. Deviation (s)	0.16	0.11	0.15
Average Depth (km)	4.6	7.5	5.4

The Challis aftershocks lasted three years (Pang et al., 2018). However, with EQT I obtain a relatively small aftershock catalog compared to Sulphur Peak and Stanley sequences. I hesitate to contribute this small catalog to the incapability of EQT's phase picking or the Hypoinverse locations given the spatial clustering results of Pang et al. (2018) are similarly reflected in the EQT results (Figure 5.7). Instead, I contribute the lack of recognized aftershocks to the poor azimuthal station coverage surrounding the epicentral region. The lack of local stations following the initiation of the second mainshock is responsible for depth bias and high uncertainty in ERZ observable in Figure 5.9. The inadequate station geometry limits the ability of EQT to match events on separate seismic stations. The high ERZ suggests that events were most likely being relocated either too close or too far from the available local station to account for travel time error as phases were detected on regional stations much farther from the aftershock hypocenters.
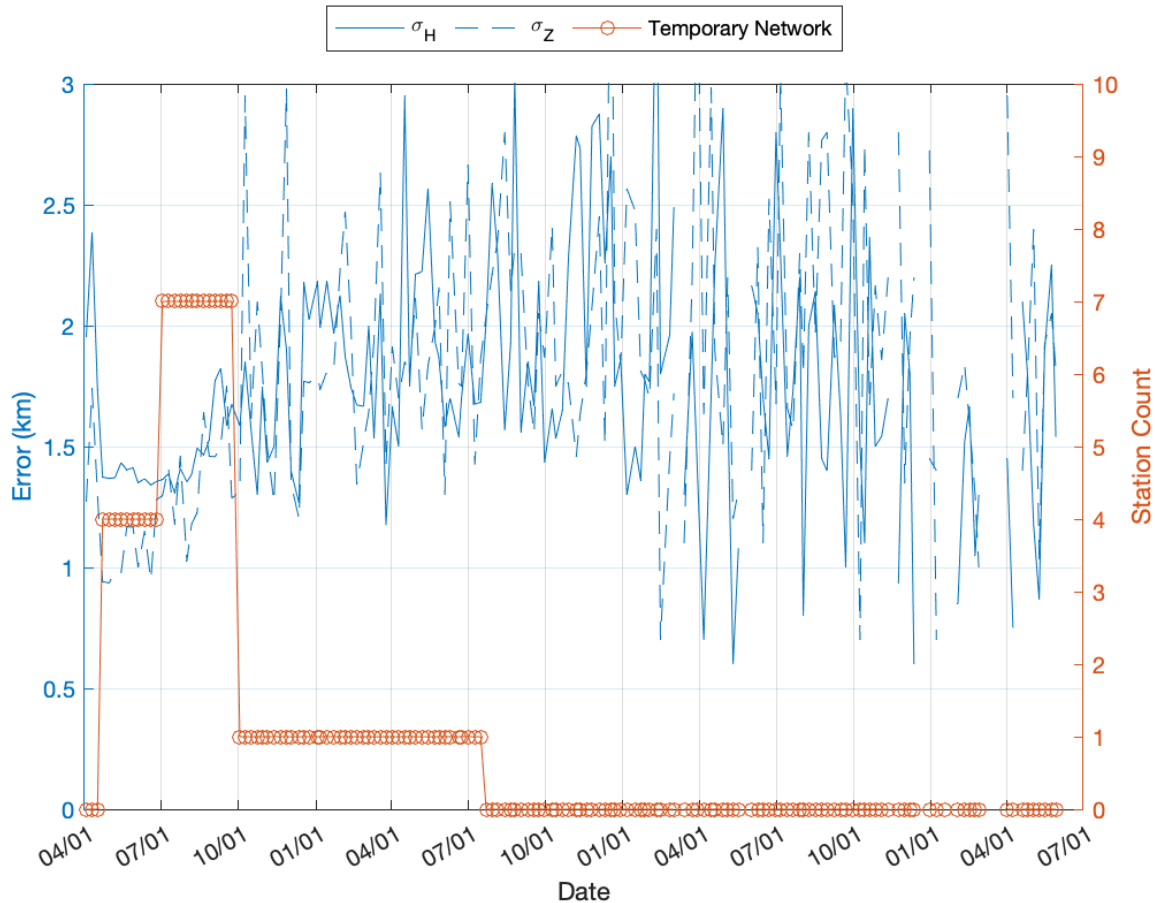
Figure 5.9 **The change in average vertical (ERZ) and horizontal (ERH) error for the Challis sequence through time (left axis). Local station count used for EQT picks through time on the right axis.**

Despite the poor local station count for half the Challis sequence duration, the total number of high-quality aftershocks detected was 2,845 using the Gradient velocity model. Using only EQT and constraining the minimum number of events in 0.5 x 0.5 km bins (Figure 5.7), I was able to replicate the spatial distribution observed by Pang et al. (2018) without using GrowClust. The GrowClust algorithm tightens aftershock distributions spatially by using nearby events as a proximal source to relocate events closer together, i.e., double-difference relocation (Trugman & Shearer, 2017). The density map shows an expected spatial distribution of events with an average RMSE of 0.09 seconds (Figure 5.7). The maximum depth of the seismogenic zone is ~15-18 km

interpreted by the notable decrease in events below this depth (lower left Figure 5.7). The results of Pang et al. (2018) demonstrate that by introducing local stations they constrained ERZ to 1.4 km for 705 relocated earthquakes using HypoInverse. In this study, I used the same stations with the new Gradient velocity model to generate a catalog with two times the number of events with the same ERZ of 1.4 km.

5.2 Discussion of Hypoinverse Results using EQT Phase Picks

The cumulative number of aftershocks in the Stanley sequence increased by a factor of five with my catalog compared to the USGS catalog. Apart from the Stanley sequence, Sulphur Peak and Challis provided results that honor the work of Koper et al. (2018) and Pang et al. (2018) while providing insight into the factors that negatively affect EQT performance. The Sulphur Peak and Challis sequence results show that EQT picks are well suited for the application of HypoInverse. This holds as long as an appropriate velocity model is used to locate the EQT picks. Hypoinverse relies heavily on a 1-D-velocity model to obtain appropriate hypocenter locations and the results obtained using the Gradient and Brumbaugh velocity models provide relatively low residual errors and high spatial certainties. However, the low residuals of the Gradient model when used to locate Sulphur Peak picks suggests that the velocity model used in Koper et al. (2018) could be improved. Future work utilizing an inverse velocity tomography approach could help to constrain the location of earthquakes for all sequences in this study; potentially helping to determine the driving mechanisms related to seismicity in each region.

In the case of Sulphur Peak, the limited number of matched USGS events found in the EQT catalog did not affect the observed spatial distribution of aftershocks. See Appendix E for a complete comparison of the spatial distribution for each sequence using

the local and AK-135f velocity models, as well as USGS picks using the AK-135f model. Using the Brumbaugh velocity model, the EQT aftershock catalog contained twice as many hand-picked aftershocks compared to the Koper et al. (2018) catalog which contained 1,048 events. The cause for the low percentage of matched EQT and USGS hypocenters is further discussed in Chapter 6.

In the case of Challis, my results show that local station count alongside an appropriate velocity model is a critical factor in the success of utilizing EQT. Despite having the sparsest local seismic network, EQT managed to provide more high-quality events and maintain a low average ERZ. Pang et al. (2018) used the local network to detect what they considered to be 705 earthquakes with good location certainty and an average ERZ of 1.4 km. Using the same local station data and the Gradient model, EQT detected 2,845 events, over three times as many, and had the same ERZ. In conclusion, EQT performed well and should be considered as an opportunistic tool in the realm of automated seismic event detection and phase picking, but this should not negate the fact that an accurate velocity model is still needed for hypocenter estimation.

In the following chapter, I explore the Stanley catalog and constrain the spatial certainty to ERZ ≤1 km and ERH ≤0.5 km to interpret aftershock patterns. Utilizing the highly constrained hypocenters, I provide a geologic interpretation of the Stanley aftershock sequence.

CHAPTER SIX: INTERPRETATION

6.1 Stanley Mainshock Characteristics

The Stanley mainshock that initiated on March 31, 2020, was initially located by

the USGS using the AK-135f velocity model and a sparse array of regional seismometers

(U.S. Geological Survey, 2022b). Within the USGS catalog, a epicentral location

uncertainty of $\pm$ 8.5 km and a depth uncertainty of $\pm$ 3.8 km was estimated. This

uncertainty prompted the Montana Bureau of Mines and Geology to relocate the

mainshock using 62 regional seismic stations and a regional velocity model obtained

from Bremmer et al. (2019). They constrained the epicentral location uncertainty to $\pm$ 0.7

km and a depth uncertainty of $\pm$ 3.8 km (U.S. Geological Survey, 2022a). The moment

tensor solution obtained from the University of Utah Seismograph Stations (U of U

Seismograph Stations, 2022) suggested left-lateral strike slip motion, consistent with that

obtained from a similar analysis by St. Louis seismologists (Saint Louis University

Moment Tensors Determinations, 2022).

6.2 Stanley Aftershock Patterns

The 15,040 EQT aftershocks obtained with my gradient velocity model with

depth errors <1 km and horizontal errors <0.5 km are shown in Figure 6.1. This map

provides the most current hypocentral distribution for the Stanley sequence to date. The

map contains two mainshock locations, the USGS and the alternative Montana Bureau of

Mines. Comparison of the USGS catalog to the EQT catalog shows an average shift of

epicenters to the southeast by ~7 km using only low residual error events. The low residual error events had an average depth uncertainty of ±1.2 km and average horizontal uncertainty of ±0.7 km, significantly less than the ±3.8 km depth uncertainty and the same horizontal uncertainty associated with the Montana mainshock location (U.S. Geological Survey, 2022a). Using this estimated bias, I relocate the mainshock location by ~7 km to the southeast (159°) of the Montana epicenter, aligning the mainshock within a dense zone of seismicity focused along an 82-degree west dipping N10W trending fault (cross section A-A' on Figure 6.1) that I term the Cape Horn fault. These aftershocks extend 30 km to the north from near the northern termination of the Sawtooth fault. These aftershocks are focused between 6 and 15 km depth. I interpret this aftershock alignment as a new fault because of the aftershock alignment along a steep west-dipping trend that is opposite the dip direction of the northwest-trending Sawtooth fault (Liberty et al., 2021). There are no known scarps or other geophysical expressions that align with the Cape Horn fault.

Another aftershock cluster is highlighted with cross-section B-B' (Figure 6.1). I map these aftershocks mostly between 4 and 10 km depth, and these aftershocks align along a west-dipping ~79-degree fault plane. Assuming a northeast dip for the Sawtooth fault, the aftershocks define a west-dipping antithetic fault to the Sawtooth fault. Connecting the surface trace location of the Sawtooth fault with the termination in seismicity along B-B' places a 67-degree northeast dip on the Sawtooth fault, consistent with previous fault dip estimates (e.g., Thackray et al., 2013). The aftershocks associated with B-B' extend approximately 5 km in length, consistent with a M5 earthquake (Wells & Coppersmith, 1994). While the largest reported aftershock in this region was M3.6

(U.S. Geological Survey, 2022a), a larger earthquake along this fault may trigger motion on the related Sawtooth fault.

I note two aftershock clusters to the south of most aftershocks and to the west of the Sawtooth fault (Figure 6.1). These zones of seismicity host multiple M>3 aftershocks, including one reported M4.4 event (U.S. Geological Survey, 2022a). My hypocenter locations for these aftershock clusters lie between 8 and 10 km depth and are focused in the footwall (west) block of the Sawtooth fault. Despite being isolated zones of seismicity, they align with the apparent N10W trending aftershock alignment (Figure 6.1).

The seismicity near the northern termination of the Sawtooth Fault is best represented by a complex interplay of small length faults of various trends. Perhaps with a more accurate 3-D velocity model, aftershock alignments would improve a multi-fault model in this area. While the Sawtooth Fault lies directly south of this energetic region, no aftershocks align along an east dipping fault; implying that the Sawtooth fault did not move during this nine-month window.
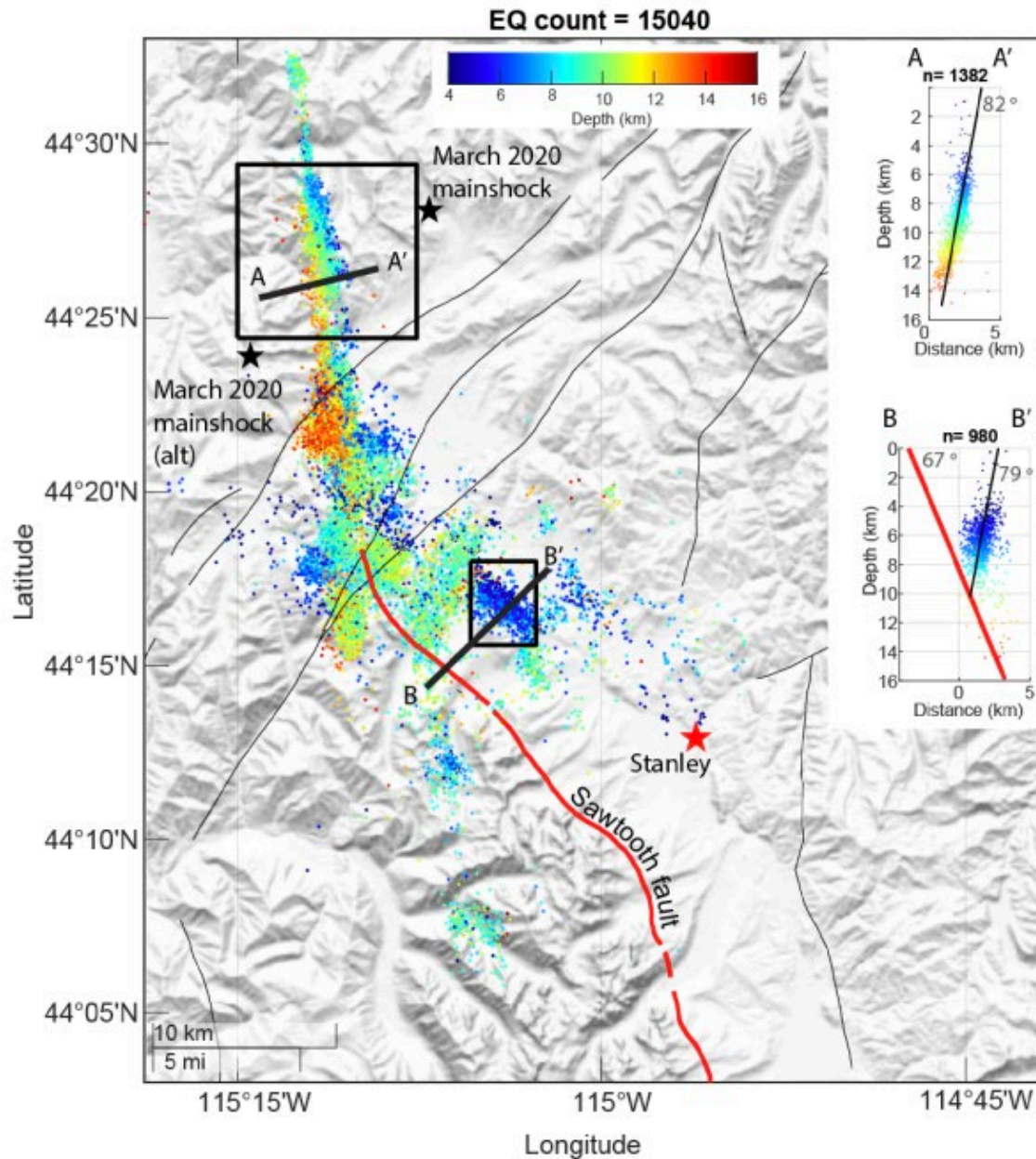
Figure 6.1 **Earthquakes color coded by depth for 15,040 high-quality events in the Stanley aftershock sequence. The two cross sections shown on the right of the image labeled A-A` and B-B` are seen in map view within the black bounding boxes. The north-eastern star represents the USGS mainshock location (U.S. Geological Survey, 2022a), the north-western most star is the Montana mainshock location. The red star to the south is the town of Stanley, ID. The thin black lines indicate the TCFS from Lewis et al. (2012).**

6.3 Fault Interplay

Figures 6.2 and 6.3 show that seismicity follows apparent trends. The heat density map shown in Figure 6.2, defined by a bin size of 0.5 km by 0.5 km, exhibits aftershock clusters that may be controlled by faults related to the TCFS. If true, this indicates that further investigation into the role of relic faults is warranted, but this is beyond the scope of my thesis research. For example, the presence of hot springs aligned with structures related to the TCFS may suggest that seismicity has promoted upward flow of hydrothermal fluids from great depths (e.g., Killsgard et al., 1986). Whether related or not, the question remains what are the driving mechanisms for fault motions and aftershock patterns in this area?
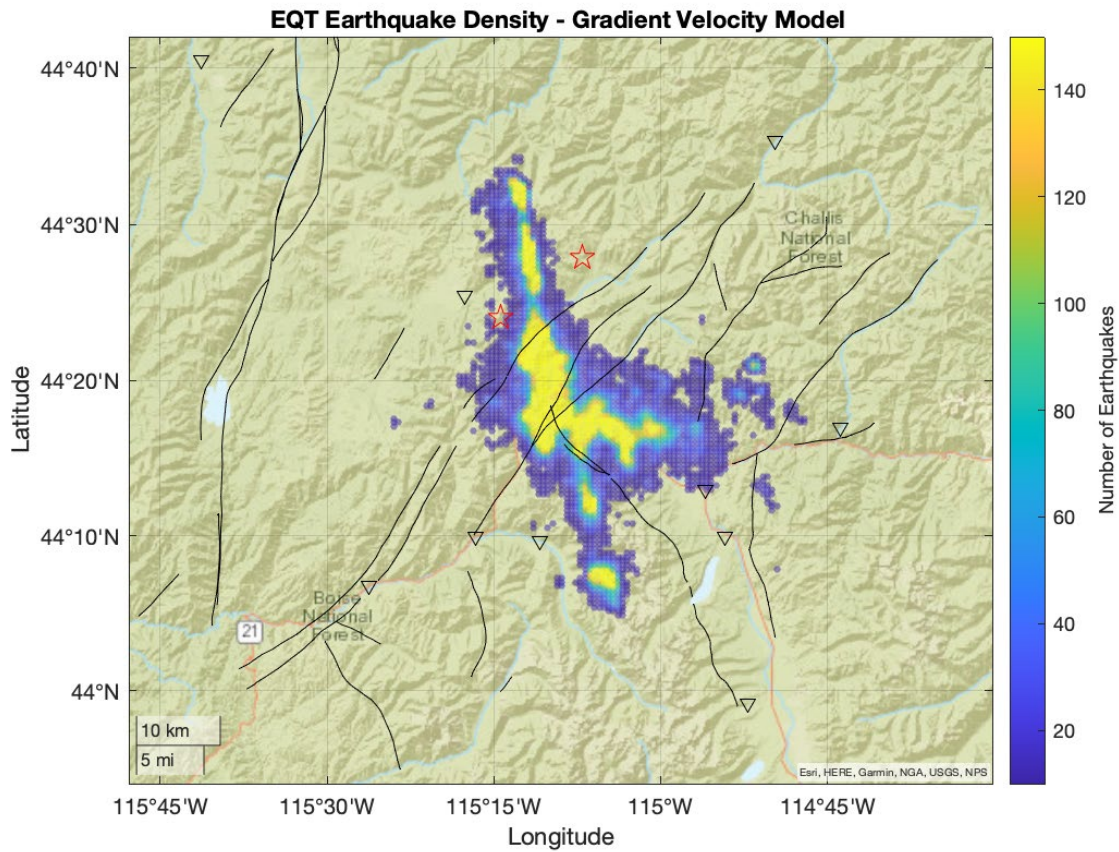
Figure 6.2   Earthquake density map and intersecting faults for the Stanley aftershock sequence. The northeastern red star represents the USGS mainshock location, the north-western most red star is the Montana mainshock location. The black triangles represent the temporary seismic stations. The thin black lines are the faults in the area (Lewis et al., 2012; U.S. Geological Survey, 2022c).
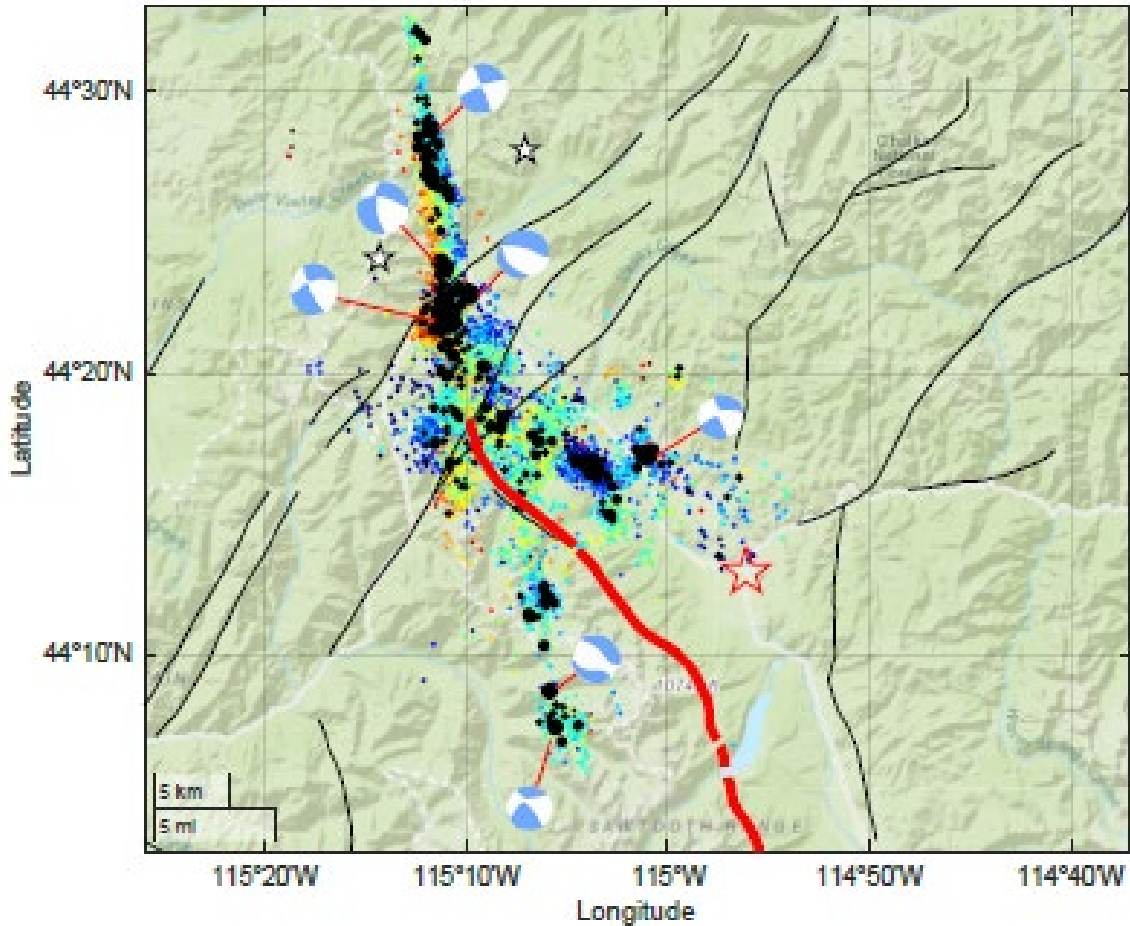
Figure 6.3   Earthquakes color coded by depth using the same scale as Figure 6.1. The black dots are EQT event locations corresponding to USGS events. The moment tensors are from the St. Louis University moment tensor catalog and are all >M3.9 (Saint Louis University Moment Tensor Determinations, 2022). The red star represents the town of Stanley, ID and the two white stars to the north are the Montana (southwest) and USGS (northeast) mainshock locations. The thin black lines are the TCFS from Lewis et al. (2012) and the thick red line is the Sawtooth fault (U.S. Geological Survey, 2022c).

6.3.1 Southern Seismicity associated with the Stanley Sequence

The St. Louis moment tensor solutions relocated using the Gradient velocity

model suggests that the southernmost aftershock cluster exhibits left-lateral strike slip

motion (Figure 6.3; Saint Louis University Moment Tensors Determinations, 2022). This

reflects a general trend seen in the moment tensor solutions in Figure 6.3, but the

southern cluster is characterized by aftershocks aligned along a vertical plane. The reason

for this alignment within the Sawtooth fault's footwall block is not clear, but by investigating the temporal distribution of this cluster and using Bäths law (Bath et al., 1965) to estimate the rate of seismicity, it may be possible to hypothesize the type of driving mechanisms that are present, i.e., coseismic or fluid-driven afterslip. Unlike the southern portions of isolated seismicity, the seismicity to the north is occurring on the a previously unmapped fault and exhibits expected aftershock alignment along its N10W strike and west dipping plane.

6.3.2 Northern Seismicity associated with the Stanley Sequence

I interpret the N10W aftershock alignment shown in Figure 6.1 as the 30 km long Cape Horn fault. The fault length to mainshock magnitude is consistent with empirical studies (Wells and Coppersmith, 1994). This observation supports the relocation of the mainshock to my new location. This fault may also have moved during the Seafoam earthquakes, as the location and magnitudes align with this aftershock trend.

Apart from the Cape Horn fault, there are intersecting planes of seismicity to the north, northeast, and southwest of the Sawtooth fault which may be the result of the intersecting TCFS. Available moment tensor solutions show that large magnitude events (M>3.9) tend to terminate where the TCFS intersects seismically active regions (Figure 6.3). There are zones of seismicity with M>3.9 events that do not intersect known relic faults, suggesting other unmapped faults in the region may exist. Therefore, the TCFS is likely playing an active role in energy migration along the unnamed faults, in hand controlling where larger earthquakes are likely to occur.

6.4 Sulphur Peak Aftershocks

My Sulphur Peak aftershock catalog contained the largest number of aftershocks that were not temporally matched to USGS aftershocks. Despite the difference in arrival times, the depth distribution shown in Figure 5.6 suggests a seismogenic zone that lies mostly above 9 km depth. Although this result is consistent with Koper et al. (2018), I note that the Gradient model places seismicity at a greater depth. The inferred shallow seismicity and overall trend of ~1km/day to the southeast (Koper et al., 2018), too fast to be considered fluid source driven (Shapiro et al., 2003), is consistent with aftershock migration driven by aseismic afterslip (Koper et al., 2018). Understanding the driving mechanism of seismicity in Sulphur Peak paired with EQT's inability to match the hand-picked phase arrivals for this sequence, suggests the neural network is not well suited to picking seismic signals caused by afterslip and should be retrained for such. Retraining EQT to match these waveforms, along with a more robust velocity model, may improve the aftershock distributions for the Sulphur Peak sequence.

6.5 Challis Aftershocks

The aftershock distribution for Challis resembled the work of Pang et al. (2018) but aftershock detection was limited by inadequate station coverage. The results obtained by EQT do not show anything that has not been previously reported, but it can be confirmed that EQT performed well when making picks using the local array of seismometers. Through EQT and Hypoinverse, I determine that the depth of the seismogenic zone is measurably deeper than the Sulphur Peak sequence and comparable to the reported depth of the Borah Peak mainshock in 1983 (Scott et al., 1985). The maximum aftershock depth lies near 15 km, similar to the Stanley sequence. Considering

the velocity models used for each sequence were the same and that both sequences lie north of the SRP, EQT exhibits consistency in its ability to detect aftershocks north of the SRP. The cause of seismicity in Challis and Stanley is still not entirely understood; however, through aftershock detection, EQT's detection mechanisms do provide insight into prior geodetic observations surrounding this region.

CHAPTER SEVEN: CONCLUSION

Machine-learning is a valuable tool capable of detecting aftershocks. EQT detected five times the number of hand-picked aftershocks for the Stanley sequence. The quick deployment of seismometers surrounding the epicentral zone of seismicity for Stanley clearly enhanced the usability and quality of EQT for seismic detection in this region.

By comparing all three aftershock sequences, I conclude that the presence of local stations is an essential component for the reliability of this automated method alongside an appropriate velocity model. Using machine-learning for seismic detection means that the construction of seismic networks needs to be carefully dictated by the capabilities of the algorithm being used. EQT eliminates the concern for picking events out of stacked phases and supports the use of dense local seismic networks rather than regional seismic arrays. These types of networks enhance the algorithms' ability to match seismic signals and minimizes the distance between stations, therefore minimizing travel time error for P- and S-wave arrivals.

Despite the increase in the number of quality events, EQT does require further attention to be used in a broader sense for seismic detection. The Sulphur Peak sequence exploits the programs' inability to identify seismic activity that is driven by afterslip. The program detected a similar number of quality events to the hand-picked Sulphur Peak catalog but only 54% of these events were associated to the origin times of events found

in the INL and USGS catalogs. The aseismic afterslip driven aftershock sequence therefore eluded EQT and proved that the program is most well suited for a tectonically driven earthquake, at least using the pre-trained version available on GitHub.

The coseismic nature of Challis and the number of events detected by EQT, as well as the temporal and spatial distribution of quality events are comparable to the work completed by Pang et al. (2018). The second sequence of events that initiated in early January of 2015 was poorly represented and can be directly correlated to the lack of local stations (Figure 5.9). Despite poor station coverage near Challis, EQT managed to provide a complete catalog of aftershocks that encompassed 85% of the total hand-picked catalog and maintain the same average ERZ reported by Pang et al. (2018) with over three times the number of detected events. I conclude that provided seismicity is due to active tectonism and constrained using a local and regional network, EQT is a viable tool to aid in aftershock detection and assist in determining the driving mechanisms for seismicity.

The updated Stanley catalog outlines a predominant N10W west dipping fault that I term the Cape Horn fault that extends for approximately 30 km. The relationship between subsurface fault length and magnitude (Wells and Coppersmith, 1994) suggests that the Cape Horn fault is responsible for the M_w 6.5 earthquake that occurred in March 2020.

Future work that would benefit this thesis would be an improved velocity model for all aftershock sequences. Also, gravity and magnetic data may assist in the understanding whether a complex relationship between subsurface fault and the intersecting relic faults exists. A better structural analysis of the region encompassing

these faults is necessary to characterize the faults and determine the likelihood of future seismicity in the region. I conclude that EQT supported the geologic investigation surrounding Stanley by cataloging an immense quantity of high-quality aftershocks. The capabilities of EQT are worth further investigation but when observed within the scope of this research, the program provided 52,125 aftershocks with ≤5 km ERZ and ERH errors for Stanley and provided similar aftershock catalogs to the previous studies about Challis and Sulphur Peak. In conclusion, EQT shows promise as a qualitative and quantitative tool to assist in low signal-to-noise aftershock detection in zones of coseismic seismicity.

REFERENCES

Allen, R. (1982). Automatic Phase Pickers: Their present use and future prospects.
Bulletin of the Seismological Society of America 1982; 72 (6B): S225–S242. doi:
https://doi.org/10.1785/BSSA07206B0225

Anders, M. H., Geissman, J. Wm., Piety, L. A., & Sullivan, J. T. (1989). Parabolic
distribution of circumeastern Snake River Plain seismicity and latest Quaternary
faulting: Migratory pattern and association with the Yellowstone hotspot. Journal
of Geophysical Research, 1989, 1589, 94(B2).
https://doi.org/10.1029/JB094iB02p01589</div>

Armstrong, R.L. & Leeman, William & Malde, H.E. (1975). K-Ar dating, Quaternary
and Neogene volcanic rocks of the Snake River Plain, Idaho. Am. J. Sci.; (United
States). 275:3. 10.2475/ajs.275.3.225. (1975)

Båth, M. (1965). Lateral inhomogeneities of the upper mantle. *Tectonophysics*, *2*(6),
483–514. https://doi.org/https://doi.org/10.1016/0040-1951(65)90003-X

Bello, S., Scott, C. P., Ferrarini, F., Brozzetti, F., Scott, T., Cirillo, D., de Nardis, R.,
Arrowsmith, J. R., & Lavecchia, G. (2021). High-resolution surface faulting from
the 1983 Idaho Lost River Fault Mw 6.9 earthquake and previous events.
Scientific Data, *8*(1). https://doi.org/10.1038/s41597-021-00838-6

Beroza, G. C. (1995). Seismic Source Modeling. Review of Geophysics, Supplement,
U.S. National Report to International Union of Geodesy and Geophysics 1991-
1994, 299–308.

Bremner, P. M., Panning, M. P., Russo, R. M., Mocanu, V., Stanciu, A. C., Torpey, M., Hongsresawat, S., VanDecar, J. C., LaMaskin, T. A., & Foster, D. A. (2019). Crustal Shear Wave Velocity Structure of Central Idaho and Eastern Oregon from Ambient Seismic Noise: Results from the IDOR Project. Journal of Geophysical Research: Solid Earth, 124(2), 1601–1625. https://doi.org/10.1029/2018JB016350

Brumbaugh, D. A. (2001). The 1994 Draney Peak, Idaho, Earthquake Sequence: Focal Mechanisms and Stress Field Inversion (dissertation). Department of Geology and Geophysics, Salt Lake City, Utah.

Crone, A., & Haller, K. (1991). Segmentation and the coseismic behavior of Basin and Range normal faults: Examples from east-central Idaho and southwestern Montana, USA. *Journal of Structural Geology*, *13*, 151–164. https://doi.org/10.1016/0191-8141(91)90063-O

Dewey, J.W. (1987). Instrumental seismicity of central Idaho. *Bulletin of the Seismological Society of America, 77*, 819-836.

Di Stefano, R., Aldersons, F., Kissling, E., Baccheschi, P., Chiarabba, C., & Giardini, D. (2006). Automatic seismic phase picking and consistent observation error assessment: application to the Italian seismicity. *Geophysical Journal International*, *165*(1), 121–134. https://doi.org/10.1111/j.1365-246X.2005.02799.x

Dieterich, J. (1994). A constitutive law for rate of earthquake production and its application to earthquake clustering. *Journal of Geophysical Research*, *99*(B2), 2601–2618. https://doi.org/10.1029/93JB02581

Doser, D. I., & Smith, R. B. (1985). Source Parameters of the 28 October 1983 Borah Peak, ID, Earthquake from Body Wave Analysis. In *Bulletin of the Seismological Society of America* (Vol. 75, Issue 4).

DuRoss, C. B., Briggs, R. W., Gold, R. D., Hatem, A. E., Elliott, A. J., Delano, J., Medina-Cascales, I., Gray, H. J., Mahan, S. A., Nicovich, S. R., Lifton, Z. M., Kleber, E., McDonald, G., Hiscock, A., Bunds, M., & Reitman, N. G. (2022). How similar was the 1983 Mw 6.9 Borah Peak earthquake rupture to its surface-faulting predecessors along the northern Lost River fault zone (Idaho, USA). *GSA Bulletin*. https://doi.org/10.1130/B36144.1

Evans, J., Martindale, D., & Kendrick, R. (2003). Geologic Setting of the 1884 Bear Lake, Idaho, Earthquake: Rupture in the Hanging Wall of a Basin and Range Normal Fault Revealed by Historical and Geological …. *Bulletin of the Seismological Society of America*, *93*, 1621–1632.

Eaton, G. P. (1982). The Basin and Range Province: Origin and Tectonic Significance. Annual Review of Earth and Planetary Sciences, 10(1). https://doi.org/10.1146/earth.1982.10.issue-1

Havskov, J. and Ottemoller, L. (1999) Seisan Earthquake Analysis Software. Seismological Research Letters, 70, 532-534. https://doi.org/10.1785/gssrl.70.5.532

Kiilsgaard, T. H., Fisher, F. S., & Bennett, E. H. (1986). THE TRANS-CHALLIS FAULT SYSTEM AND ASSOCIATED PRECIOUS METAL DEPOSITS, IDAHO. In *Economic Geology* (Vol. 81).

Klein, F. (2014). *User's Guide to HYPOINVERSE-2000, a Fortran Program to Solve for Earthquake Locations and Magnitudes, Version 1.40*. https://doi.org/10.13140/2.1.4859.3602

Koper, K. D., Pankow, K. L., Pechmann, J. C., Hale, J. M., Burlacu, R., Yeck, W. L., Benz, H. M., Herrmann, R. B., Trugman, D. T., & Shearer, P. M. (2018). Afterslip Enhanced Aftershock Activity During the 2017 Earthquake Sequence Near Sulphur Peak, Idaho. *Geophysical Research Letters*, *45*(11), 5352–5361. https://doi.org/10.1029/2018GL078196

Lewis, R. S., P. K. Link, L. R. Stanford, and S. P. Long (2012). Geologic map of Idaho, Idaho Geol. Surv. Geol. Map 9, Scale 1:750,000.

Liberty, L. M.,Z. M. Lifton, and T. Dylan Mikesell (2021).The 31 March 2020 Mw6.5 Stanley, Idaho, Earthquake: Seismotectonics and Preliminary Aftershock Analysis, Seismol. Res. Lett.XX,1–16, doi:10.1785/0220200319

Montagner, J. P., & Kennett, B. L. N. (1996). How to reconcile body-wave and normal-mode reference earth models. *Geophysical Journal International*, *125*(1), 229–248. https://doi.org/10.1111/j.1365-246X.1996.tb06548.x

Mousavi, S. M., Ellsworth, W. L., Zhu, W., Chuang, L. Y., & Beroza, G. C. (2020). Earthquake transformer—an attentive deep-learning model for simultaneous earthquake detection and phase picking. *Nature Communications*, *11*(1). https://doi.org/10.1038/s41467-020-17591-w

Pang, G., Koper, K. D., Stickney, M. C., Pechmann, J. C., Burlacu, R., Pankow, K. L., Payne, S., & Benz, H. M. (2018). Seismicity in the Challis, Idaho, Region, January 2014-May 2017: Late aftershocks of the 1983 Ms 7.3 Borah Peak Earthquake. *Seismological Research Letters*, *89*(4), 1366–1378. https://doi.org/10.1785/0220180058

Payne, S. J., McCaffrey, R., & Kattenhorn, S. A. (2013). Extension-driven right-lateral shear in the centennial shear zone adjacent to the eastern snake river plain, Idaho. *Lithosphere*, *5*(4), 407–419. https://doi.org/10.1130/L200.1

Peng, Z., & Gomberg, J. (2010). An integrated perspective of the continuum between earthquakes and slow-slip phenomena. In *Nature Geoscience* (Vol. 3, Issue 9, pp. 599–607). https://doi.org/10.1038/ngeo940

Personius, S., Crone, A., Machette, M., Mahan, S., & Lidke, D. (2009). Moderate rates of late Quaternary slip along the northwestern margin of the Basin and Range Province, Surprise Valley fault, northeastern California. *Journal of Geophysical Research*, *114*. https://doi.org/10.1029/2008JB006164

Pollitz, F. F., Hammond, W. C., & Wicks, C. W. (2021). Rupture process of the M 6.5 Stanley, Idaho, earthquake inferred from seismic waveform and geodetic data. Seismological Research Letters, 699–709. https://doi.org/10.1785/0220200315</div>

Recent Earthquake Map. U of U Seismograph stations. (n.d.). Retrieved April 28, 2022, from https://quake.utah.edu/earthquake-center/quake-map

Ruhl, C. J., Abercrombie, R. E., Smith, K. D., & Zaliapin, I. (2016). Complex spatiotemporal evolution of the 2008 Mw 4.9 Mogul earthquake swarm (Reno, Nevada): Interplay of fluid and faulting. *Journal of Geophysical Research: Solid Earth*, *121*(11), 8196–8216. https://doi.org/10.1002/2016JB013399

Saint Louis University, 2022, Moment Tensors Determinations, accessed May 5th, 2022 at URL https://www.eas.slu.edu/eqc/eqcmt.html).

Scott, W. E., Pierce, K. L., & Hait, M. H. (1985). Quaternary Tectonic setting of the 1983 Borah Peak Earthquake, Central Idaho. In *Bulletin of the Seismological Society of America* (Vol. 75, Issue 4).

Shapiro, S., Patzig, R., Rothert, E. et al. Triggering of Seismicity by Pore-pressure Perturbations: Permeability-related Signatures of the Phenomenon. Pure appl. geophys. 160, 1051–1066 (2003). https://doi.org/10.1007/PL00012560

Shemeta, J. E. (1989). New analyses of three-component digital data for aftershocks of the 1983 Borah Peak, Idaho, earthquake: Source parameters and refined hypocenters, M.S. Thesis, Department of Geology and Geophysics, University of Utah.

Smith, R. B., & Sbar, M. L. (1974). Contemporary Tectonics and Seismicity of the Western United States with Emphasis on the Intermountain Seismic Belt. *GSA Bulletin*, *85*(8), 1205–1218. https://doi.org/10.1130/0016-7606(1974)85<1205:CTASOT>2.0.CO;2

Stickney, M. C., & Bartholomew, M. J. (1987). Seismicity and Late Quaternary Faulting of the northern Basin and Range Province, Montana and Idaho. In *Bulletin of the Seismological Society of America* (Vol. 77, Issue 5).

Thackray, G. D., Rodgers, D. W., & Streutker, D. (2013). Holocene scarp on the sawtooth fault, central Idaho, USA, documented through lidar topographic analysis. *Geology*, *41*(6), 639–642. https://doi.org/10.1130/G34095.1

Trnkoczy, A. (2009). *Understanding and parameter setting of STA/LTA trigger algorithm*.

Trugman, D. T., & Shearer, P. M. (2017). GrowClust: A Hierarchical clustering algorithm for relative earthquake relocation, with application to the Spanish Springs and Sheldon, Nevada, earthquake sequences. *Seismological Research Letters*, *88*(2), 379–391. https://doi.org/10.1785/0220160188

U.S. Geological Survey, (2022a), Earthquake Lists, Maps, and Statistics, accessed May 5, 2022 at URL https://www.usgs.gov/natural-hazards/earthquake-hazards/lists-maps-and-statistics).

U.S. Geological Survey (2022b). Comprehensive earthquake catalog, available at URL https://earthquake.usgs.gov/earthquakes/search/ last accessed May 5, 2022).

U.S. Geological Survey, (2022c), Quaternary Faults and Folds Database, accessed May 5, 2022 at URL https://www.usgs.gov/programs/earthquake-hazards/faults

University of Utah, 2022, U of U Seismograph Stations, accessed August 1, 2022, at URL https://quake.utah.edu

Wells, D. L., & Coppersmith, K. J. (1994). New Empirical Relationships among Magnitude, Rupture Length, Rupture Width, Rupture Area, and Surface Displacement. In *Bulletin of the Seismological Society of America* (Vol. 84, Issue 4).

APPENDIX A

Depth Correction

Depth Correction Process

The 1D velocity model used in the event relocations was a homogenous crustal model, designated by the command 'CRH' in the Hypoinverse 'inlloc' file. 'CRH' models compute location depths relative to the top of the datum, which varied for each velocity model tested. It is important to note when using Hypoinverse that using a CRH model will only output depths relative to the datum as positive depths. Each velocity model in this study represents elevation above sea level as a negative depth; however, the datum for each pick was determined by averaging the elevation of the five nearest stations to an earthquake. This average station elevation is the geoid depth or surface elevation relative to a single aftershock. Therefore, depths had to be transformed from the relative datum to the velocity model datum by subtracting the 'CRH' depth datum, outputted in the 'arc' file form the model depth in the 'sum' file of Hypoinverse. (Klein, 2014). The depth datum is divided by 1000 to convert from meters to kilometers. A graphic representation of each layer is provided in Figure A.1.

The relationship is as follows:

$$Event\ Depth\ (km\ below\ ground)$$

$$= Model\ Depth\ (km\ below\ surface) - \frac{Depth\ Datum}{1000}$$
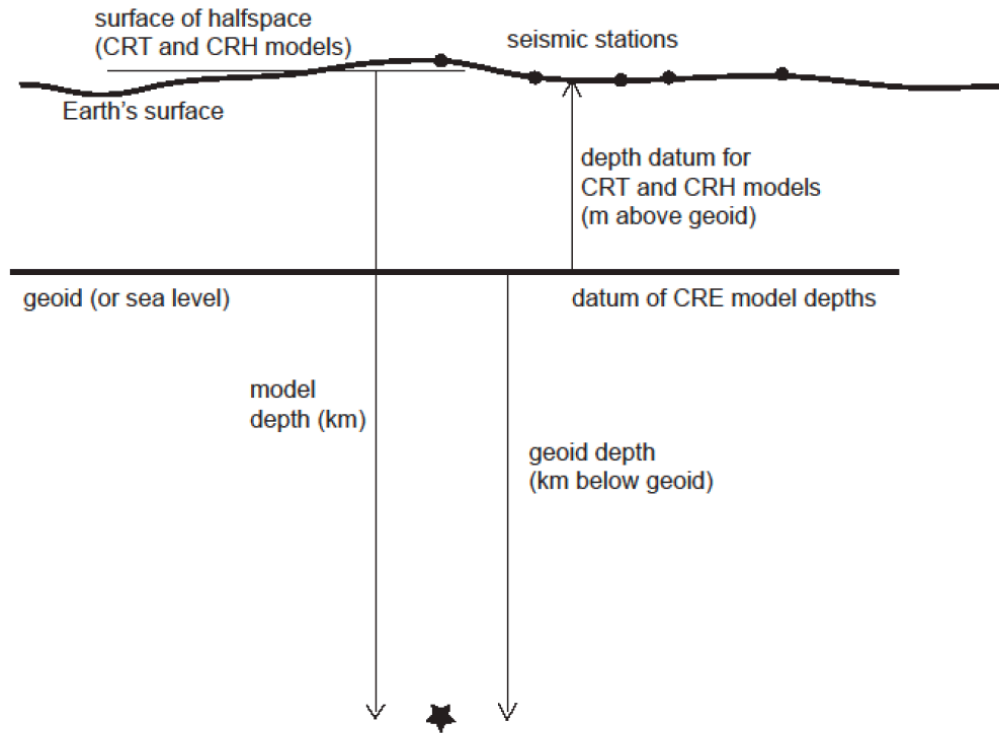
Figure A.1 **The representation of relative depths using velocity model depth datum, seismic stations, sea level represented as geoid depth, and datum depth represented as station elevation. The figure is from the Hypoinverse 1.4 Manual (Klein, 2014).**

APPENDIX B

The EQT Workflow

EQT Workflow Process

The first step in parameterizing machine-learning code is defining a minimum and maximum latitude and longitude as well as a start and stop time for temporal and spatial bounds used in data retrieval. Within these bounds EQT relies on the IRIS data management center (DMC) to determine whether data exists. If the data exists, it retrieves three-channel component seismic data on any available stations within the spatial bounds and creates a station list that is sorted in the current directory and called later. The number of processors used for data processing must be set within the data retrieval step, this simply controls the time it will take to process all the data for a given sequence. It is important to note that for large volumes of data it is beneficial to run the code in monthly chunks and then concatenate the output files. This is especially beneficial if the number of available processors is limited.

Once the date has been retrieved using an available DMC client, EQT begins a preprocessing step to prepare the metadate for event detection. The downloaded miniseed files are used directly for detection and phase picking. There is a separate option that allows the user to test how well the EQT model is performing on a snippet of the data. In this thesis I performed detection and phase picking directly on the miniseed data because it saves processing time and space by not creating an hdf5 file for event traces. The authors of EQT recommend this method for larger datasets and in this thesis each sequence exceeded a terabyte.

Once the DMC client is chosen, the method for pre-processing is chosen, an EQT trained input model is defined, and the user defined inputs for overlapping window time

(seconds) and P-/S-wave amplitude picking is set, the code is almost ready to be ran. The last step is phase association necessary to determine the nature of the arriving phases.

Here lies one critical difference between a human picking phase arrivals and a machine. A human can determine the impulsive or emergent nature of an arrival by looking at the signal directly. EQT requires an additional step, and this is controlled by the phase association function within the script. The output file, Y2000.phs, must be created first for the traces and phases to be stored within a file and not to the current directory. Once the empty output file is created the phase association step is implemented and the output file is readily transferrable to a traditional relocation algorithm such as HypoInverse (Mousavi et al., 2020). Figure B.1 shows the general workflow from obtaining seismic data to cataloging hypocenters.

The programmatic parameters for phase association and event detection were as follows:

1.) Minimum number of stations needed for event detection equals three.

2.) A preset overlapping window of 0.3 seconds used for template matching of potential events.

3.) A P-wave probability threshold of 0.1 amplitude, S-wave probability threshold of 0.1 amplitude.

4.) A probability detection threshold of 0.3 for the hierarchical attentive processing of EQT.
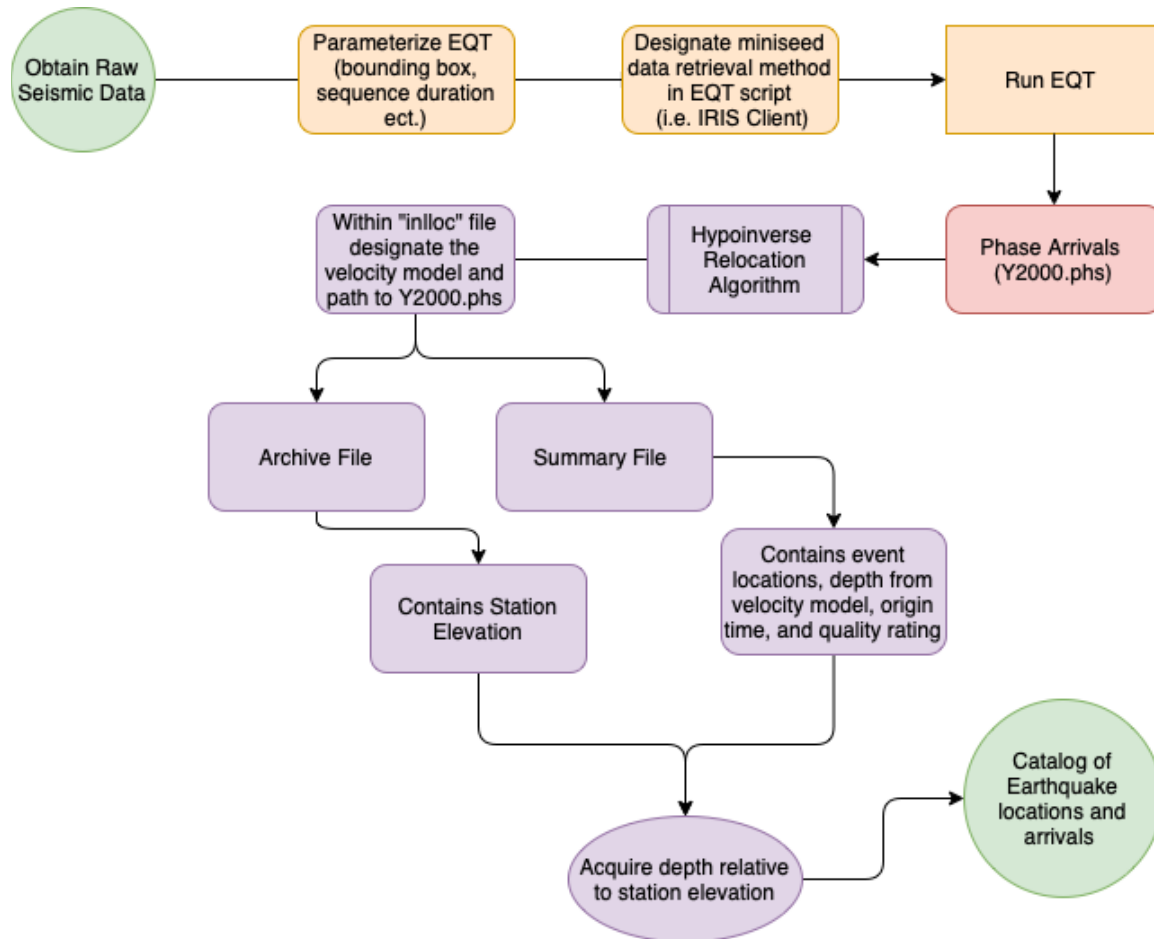
Figure B.1   Workflow diagram.

Table B.1   Catalog Characteristics Table

Characteristic	Stanley	Sulphur Peak	Challis
Main shock t_0	2020-03-31T23:52:31 UTC	2017-09-02T23:56:53 UTC	2014-04-13T00:04:39 UTC
Main shock(s) magnitude	M_l 6.5	1st: M_w 4.9 2nd: M_w 5.3	1st: M_l 4.5 2nd: M_l 5.0
Main shock (lat, lon)	44.484°, -115.1361°	42.647°, -111.449°	44.62°, -114.33°
Sequence start date	2020-03-31	2017-09-01	2014-04-17
Station bounding box [deg] [lat_{min}, lat_{max}, lon_{min}, lon_{max}]	[41.46, 47.46, -117.64, -112.64]	[41.80, 43.56, -113.15, -110.10]	[43.00, 45.50, -115.00, -111.70]
Number of Events (**EQT**)	74672	2946	5614
Number of Events < 5km Vertical / Horizontal Error (i.e., quality events)	52125	2170	2845
Mean depth [km] (**EQT** quality events)	8.5	5.8	7.0

Characteristic	Stanley	Sulphur Peak	Challis
Mean horizontal error [km] (**EQT** quality events)	0.7	0.9	1.6
Mean vertical error [km] (**EQT** quality events)	1.2	0.8	1.4
Mean depth [km] (**USGS**)	8.7	8.0	8.9
Mean horizontal error [km] (**USGS**)	2.21	1.5231	2.66
Mean vertical error [km] (**USGS**)	3.35	3.87	5.04
Percentage of Events located by **EQT** in **USGS** catalog	89%	53%	85%
Percentage of Events located by **EQT** in **INL** catalog	97%	57%	84%

APPENDIX C

Local Network Stations

Table C.1   Stanley Temporary Network/Stations

Network	Station	Latitude	Longitude	Site Name	Start Time	End Time
XP	BANN	44.303339	-115.23458	Banner Summit	2020-04-01T20:50:32	2021-05-19T00:37:25
XP	DDR	44.588581	-114.82811	Diamond Ranch	2020-04-09T21:12:50	2020-10-26T18:54:04
XP	EPIC	44.394424	-115.17500	Epicenter	2020-04-01T23:30:34	2020-10-18T20:57:45
XP	FOX	44.166052	-115.27810	Fox Creek	2020-04-01T21:56:39	2021-05-19T01:21:18
XP	IRON	44.220541	-114.98112	Iron Creek	2020-04-02T03:14:01	2020-10-18T19:06:30
XP	MFRD	44.423645	-115.29398	Middle Fork Road	2020-04-05T19:08:24	2020-10-15T19:44:03
XP	PARK	44.274849	-115.01898	PARK	2020-04-13T17:13:06	2020-06-13T00:41:00
XP	PETL	43.986603	-114.86994	Pettit Lake	2020-04-12T00:13:20	2020-10-28T19:08:30
XP	RDFL	44.165629	-114.90439	Red Fish Lake	2020-04-11T22:50:00	2020-10-28T20:09:23
XP	SAC	44.160875	-115.18114	Sacajawea Hot Springs	2020-04-01T20:44:05	2020-10-15T17:27:23
XP	SUNB	44.282725	-114.73131	Sunbeam	2020-05-08T20:28:40	2020-10-28T17:50:51
XP	TCK	44.721792	-115.00560	Thomas Creek Ranch	2020-04-09T23:05:50	2020-10-26T17:30:27
XP	TRAP	44.319286	-115.09571	Trap Creek Campground	2020-04-02T02:14:13	2020-05-30T20:13:55
XP	TRP2	44.319394	-115.10057	Trap Creek Campground 2	2020-04-02T20:23:26	2020-05-30T19:48:42
XP	WARM	44.674593	-115.68838	Warm Lake	2020-04-10T19:43:50	2020-10-25T22:54:54
GS	ID11	44.11278	-115.43722	Stanley	2020-04-05T00:00:00	2021-05-26T19:00:00

Table C.2 Sulphur Peak Temporary Networks/Stations

Network	Station	Latitude	Longitude	Site Name	Start Time	End Time
GS	ID05	42.6429	-111.459	Sulphur Canyon Road, , ID, USA	2017-09-07 19:05:00	2017-10-24 16:15:00
GS	ID06	42.5852	-111.4518	Fossil Canyon, Idaho, USA	2017-09-08 00:00:00	2017-10-24 18:55:00
GS	ID07	42.5349	-112.0797	Smith Canyon Rd., Idaho, USA	2017-09-08 21:40:00	2017-10-25 18:28:00
GS	ID08	42.8966	-111.8389	Devils Gate, Idaho, USA	2017-09-09 00:00:00	2017-10-25 20:14:00
GS	ID09	42.2444	-111.1936	Alton, Idaho, USA	2017-09-09 18:00:00	2017-10-26 16:40:00
GS	ID10	44.5183	-110.8919	Lander Cutoff, WY, USA	2017-09-12 23:00:00	2017-10-26 18:10:00

UU	ASI4	42.6567	-111.6032	Soda Springs, ID	2017-09-05 00:00:00	2019-06-13 23:59:59
UU	ASI5 (ASI6)	42.4775 (42.476)	-111.3694 (-111.3694)	Georgetown, ID	2017-09-06 00:00:00	2017-12-04 23:59:59

Table C.3   Challis Temporary Networks/Stations

Network	Station	Latitude	Longitude	Site Name	Start Time	End Time
GS	ID01	44.4356	-114.1499	Challis, ID	2014-04-17 00:00:00	2014-09-24 14:09:00
GS	ID02	44.6047	-114.1844	Challis, ID, 7.5mi N off of Rte 9	2014-06-25 00:00:00	2014-09-25 00:11:00
GS	ID03	44.4534	-113.8789	East of Route 461 near Challis, ID, USA	2014-06-25 00:00:00	2014-09-25 00:11:00
GS	ID04	44.8456	-114.2429	Mogan Creek Rd Rte 129, ID, USA	2014-06-25 00:00:00	2014-09-25 00:11:00
IE	DVCI	44.3736	-113.9991	Devils Canyon	2015-06-24 00:00:00	OPEN
UU	ASI1	43.9290	-114.729	Bonanza, ID, U.S.A.	2014-04-18 00:00:00	2014-09-23 23:59:59

| UU | ASI2 | 44.5744 | -114.2577 | Darling Creek, Challis, ID, USA | 2014-04-17 00:00:00 | 2015-07-14 23:59:59 |
| UU | ASI3 | 44.5047 | -114.2299 | Challis, ID, USA | 2014-04-16 00:00:00 | 2014-09-24 23:59:59 |

APPENDIX D

Velocity Models

Below are the various velocity models I tested during the process of selecting the final velocity models.

Table D.1   AK-135f Velocity Model

Layer	Depth of Top of the Layer[a] (km)	P-Wave Velocity (km)
1	-3.00	5.8
2	20.00	5.8
3	20.10	6.5
4	35.00	6.5
5	35.10	8.04
6	77.50	8.045

[a]*The datum is set to be 3.10 km above sea level for this model*

The Vp/Vs ratio for this model 1.69.

Table D.2   Gradient Velocity Model

Layer	Depth of Top pf the Layer[a] (km)	P-Wave Velocity (km)
1	-3.00	5.8
2	20.00	6.5
3	35.00	8.04
4	77.5	8.05

[a]*The datum is set to be 3.10 km above sea level for this model.*

The Vp/Vs ratio for this model 1.69.

Table D.3   Sulphur Peak Velocity Model

Layer	Depth of Top pf the Layer[a] (km)	P-Wave Velocity (km)
1	-2.29	1.9
2	-2.09	4.7
3	-0.29	5.1
4	1.31	5.6
5	2.91	6.1
6	4.71	6.2
7	19.71	6.8
8	39.17	7.9

[a]*The datum is set to be 2.29 km above sea level for this model.*

The Vp/Vs ratio for this model 1.73

Table D.4   Challis Velocity Model

Layer	Depth of Top pf the Layer[a] (km)	P-Wave Velocity (km)
1	-3.10	4.75
2	-0.36	5.72
3	4.95	6.06
4	16	6.80
5	38	8.00

[a]*The datum is set to be 3.10 km above sea in this model.*

The Vp/Vs ratio for this model is 1.74.

APPENDIX E

Other EQT Catalog Results
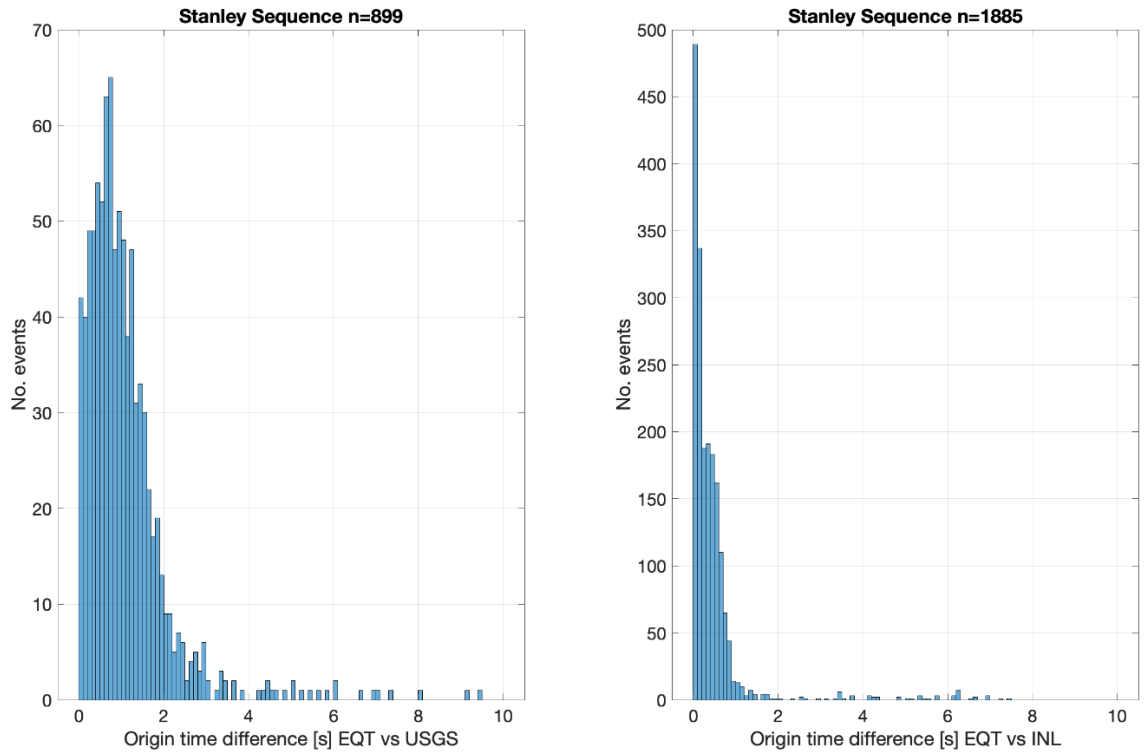
Figure E.1   Origin time difference between EQT picks and USGS (left) and INL (right) Stanley catalogs. The letter "n" represents the total number of events found by EQT in either the USGS or INL catalog.
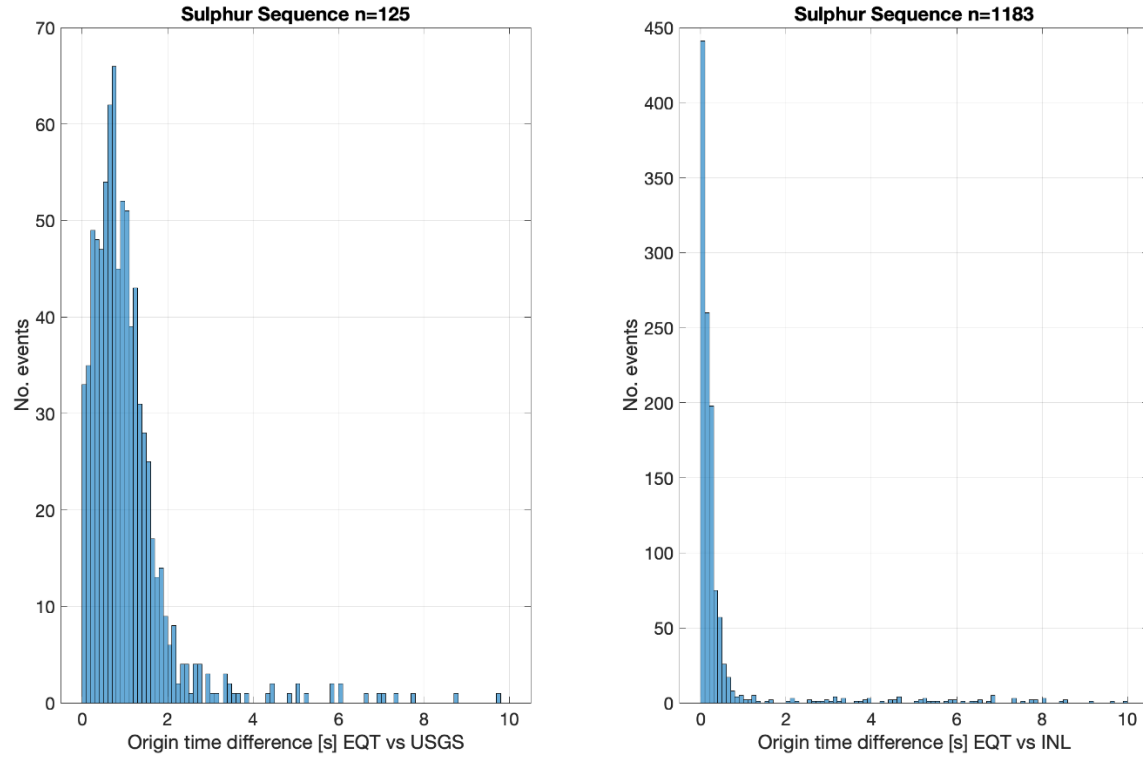
Figure E.2 Origin time difference between EQT picks and USGS (left) and INL (right) Sulphur Peak catalogs. The letter "n" represents the total number of found by EQT in either the USGS or INL catalog
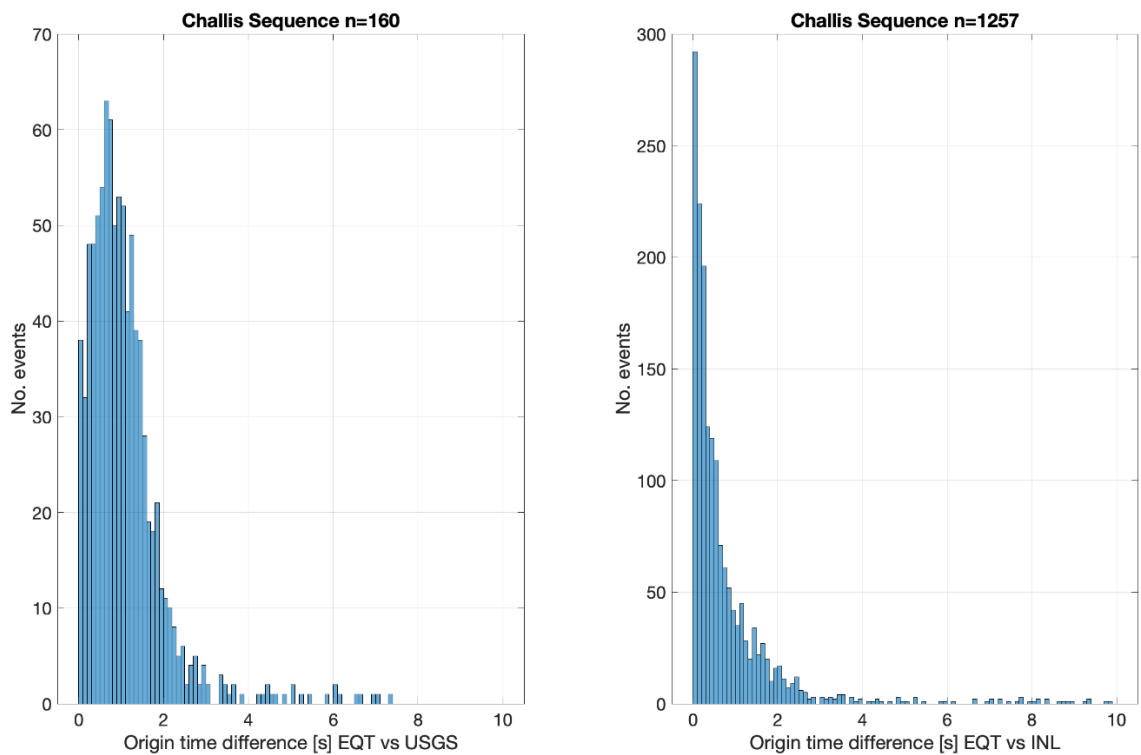
Figure E.3   Origin time difference between EQT picks and USGS (left) and INL (right) Challis catalogs. The letter "n" represents the total number of found by EQT in either the USGS or INL catalog.
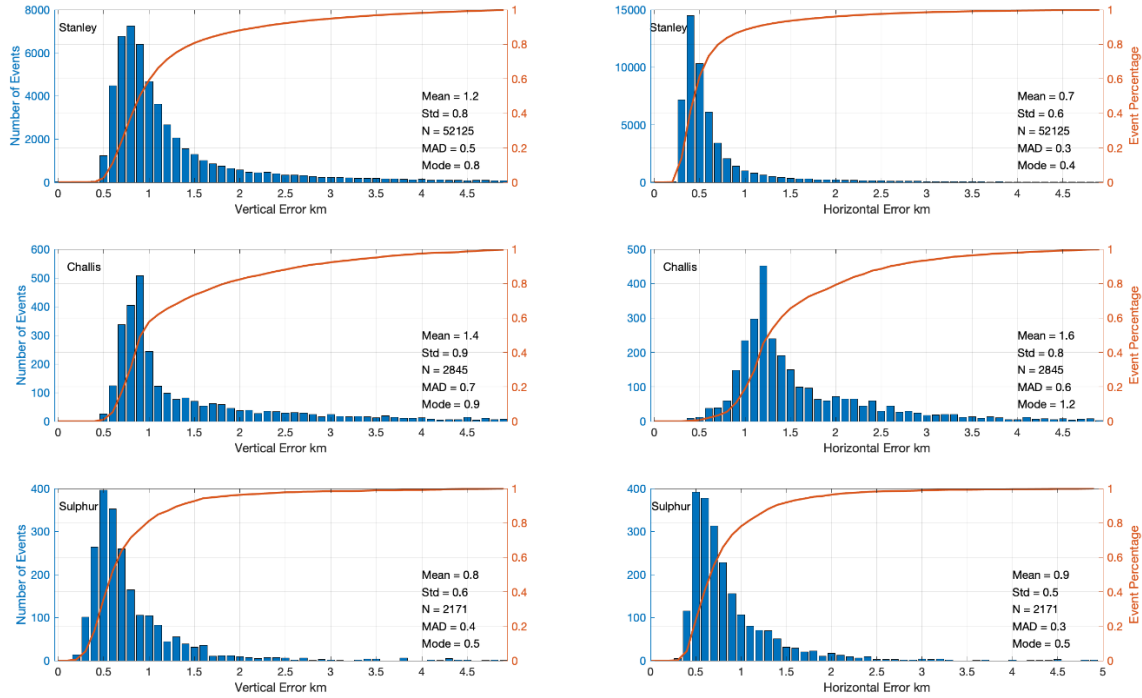
Figure E.4 **The left column of histograms shows the ERZ and the right shows ERH in bins of 0.1km. The rows from top to bottom are Stanley, Challis, and Sulphur Peak. The orange line on each plot shows the cumulative number of events at any point in time with the right axis being the percentage of total events in the EQT catalog. The data being shown is from Hypoinverse relocations using my velocity model for Stanley and Challis sequences and the Brumbaugh model for the Sulphur Peak sequence.**
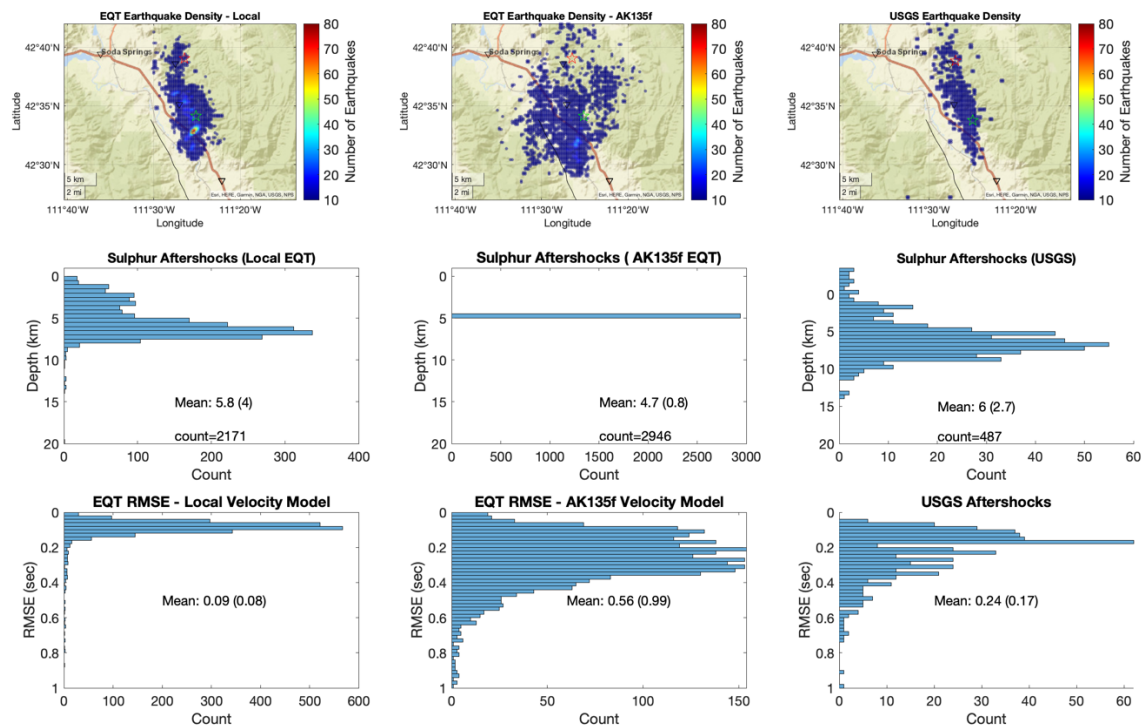
Figure E.5   Earthquake density plots of Sulphur Peak sequence are shown above. The first column represents the EQT picks with a localized velocity model from Brumbaugh (2001), the middle column shows EQT picks with the AK135f model, and the last column shows the USGS catalog. The bins for earthquake density are 0.25 x 0.25 km horizontal bins. The black line is the EBLF (U.S. Geological Survey, 2022c). The highest density per bin is set to be 80 earthquakes for the first two columns tested by EQT. The middle row represents aftershock depth distribution, the labels are the mean, followed by the standard deviation, and the total number of events. The last row shows the travel time residual error for each column accompanied by the mean and standard deviation.
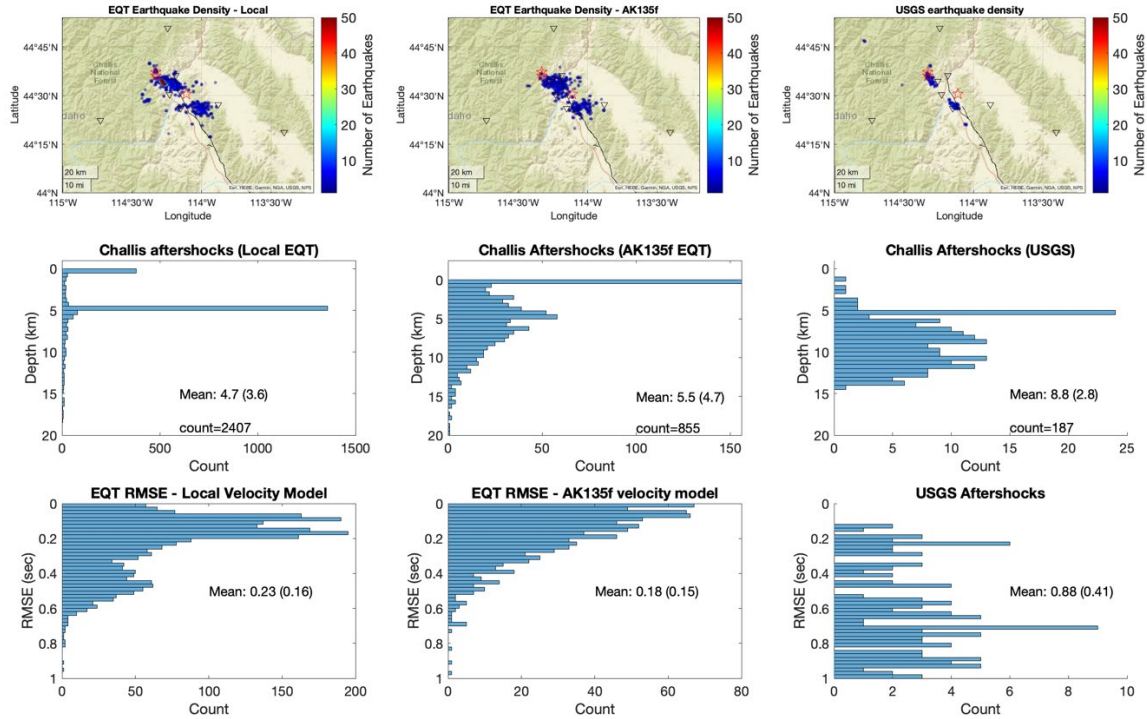
Figure E.6 **Earthquake density plots of Challis sequence are shown above. The first column represents the EQT picks with a localized velocity model from Shemeta (1989), the middle column shows EQT picks with the AK135f model, and the last column shows the USGS catalog. The bins for earthquake density are 0.5 x 0.5 km horizontal bins. The highest density per bin is set to be 80 earthquakes for the first two columns tested by EQT. The black line is the Lost River fault (U.S. Geological Survey, 2022c). The middle row represents aftershock depth distribution, the labels are the mean, followed by the standard deviation, and the total number of events. The last row shows the travel time residual error for each column accompanied by the mean and standard deviation.**